University of BRISTOL

DEPARTMENT OF MECHANICAL ENGINEERING

The Study of Acoustic Metamaterials

Sokratis Anagnostopoulos, Rebecca Heald,
Sirui (Alick) Huang, Richard Pyle, Jinwen Zhou

Supervisor: Mahdi Azarpeyvand

Report Submitted for the Degree of Engineering June 2018

Acknowledgements

We would like to thank Mahdi Azarpeyvand for his assistance as our project supervisor, Abishek Guatam for his support and advice throughout and Weam Elsahhar for his guidance in impedance tube experimental procedure.

DECLARATION

The accompanying research project report entitled: ``The Study of Acoustic Metamaterials'' is submitted in the fourth year of study towards an application for the degree of Master of Engineering in Mechanical Engineering at the University of Bristol. The report is based upon independent work by the candidates. All contributions from others have been acknowledged above. The supervisors are identified at the start of the report. The views expressed within the report are those of the authors and not of the University of Bristol.

I hereby declare that the above statements are true.

Signed (all authors)

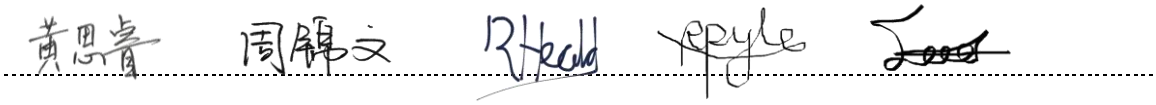

Full Names (in same order as signatures)

Sirui Huang (Alick), Jinwen Zhou, Rebecca Heald, Richard Pyle, Sokratis Anagnostopoulos

Date 13/04/2018

Declaration of Copyright

Certification of ownership of the copyright in a dissertation presented as part of and in accordance with the requirements for the Final Degree of Master of Engineering at the University of Bristol, Faculty of Engineering.

I hereby assert that I own exclusive copyright in the item named below. I give permission to the University of Bristol Library to add this item to its stock and to make it available for consultation in the library, and for inter-library lending for use in another library. It may be copied in full or in part for any bone fide library or research worker on the understanding that users are made aware of their obligations under the copyright legislation, i.e. that no quotation and no information derived from it may be published without the author's prior consent.

Authors	*Sirui Huang (Alick), Jinwen Zhou, Rebecca Heald, Richard Pyle and Sokratis Anagnostopoulos*
Title	*The Study of Acoustic Metamaterials*
Date of Submission	*17th April 2018*

Signed (all authors)

Date 13/04/2018

This dissertation is the property of the University of Bristol Library and may only be used with due regard to the author. Bibliographical references may be noted but no part may be copied for use or quotation in any published work without prior permission of the author. In addition, due acknowledgement for any use must be made.

Work Allocation

Sirui Huang (Alick)	**Jinwen Zhou**	**Richard Pyle**	**Rebecca Heald**	**Sokratis Anagnostopoulos**
Impedance tube experiments using heterogeneous metamaterials		Design and construction of square section impedance tube and 2D waveguide		Numerical simulations of square section impedance tube and 2D waveguide
Design of hybrid metamaterials and testing with impedance tube method		Impedance tube experiments using labyrinthine materials.		Numerical simulation of hybrid metamaterial
		2D waveguide experiments using labyrinthine materials.		
Post-processing of impedance tube results				Post-processing and analysis of numerical results
		Post-processing of 2D waveguide results		Analytical modelling
Comparison of experimental and numerical results				
Report writing				

I hereby confirm that the table above provides an accurate and fair representation of the allocation of work between project group members.

Signed (authors)

Full Names (in same order as signatures)

Sirui Huang (Alick), Jinwen Zhou, Rebecca Heald, Richard Pyle, Sokratis Anagnostopoulos

Summary

Acoustic metamaterials make use of precisely designed, composite structures to create unusual acoustic properties. This project studies heterogeneous, hybrid and labyrinth metamaterials to better understand how structural alterations can engineer specific acoustic properties.

Helmholtz resonator based heterogeneous metamaterials are investigated using an impedance tube. Peak absorption at specific frequencies can be targeted by changing the resonators cavity shape and neck area. Broadband frequency absorption can also be achieved using multi-band resonators. The absorption coefficient of a hybrid metamaterial is studied experimentally and confirmed numerically in 2D. It is found that hybrid metamaterials with a range of cavity volumes provides a good balance between broad range and peak absorption.

For labyrinth metamaterials, transmission loss across one unit cell and refraction angle through a 2D prism have been investigated. The findings of a previous study have been well replicated both experimentally and numerically. The frequency range of high transmission loss can be altered with changes to the labyrinth's unit cell design. 2D tests confirm numerical findings that transmission angle through a labyrinth prism is strongly dependent on the phase change through the structure.

A detailed numerical study using COMSOL satisfactorily validates the experimental findings and extends the understanding of hybrid and labyrinth metamaterials. COMSOL is used to further investigate the negative index physics behind labyrinth prisms. Finally an analytical approach is developed to describe space-coiling capabilities of a single zig-zag unit with closed-end and open-end geometry. The obtained results are close to the corresponding numerical, and are taken at negligible computational cost.

Table of Contents

List of Figures

List of Abbreviations

1 Introduction **1**
1.1 Introduction to Metamaterials . . . 1
1.2 Acoustic Metamaterials . . . 2
1.2.1 Heterogeneous Metamaterials . . . 2
1.2.2 Hybrid Metamaterials . . . 3
1.2.3 Labyrinth Metamaterials . . . 4
1.3 Objectives . . . 6

2 Experimental & Numerical Methods **7**
2.1 Circular Section Impedance Tube . . . 7
2.1.1 Two Microphone Set-up . . . 7
2.1.2 Four Microphone Set-up . . . 7
2.1.3 Impedance Tube Measurement Methods . . . 8
2.2 Square Section Impedance Tube . . . 10
2.2.1 Design & Construction . . . 11
2.3 Two-Dimensional Waveguide . . . 12
2.3.1 Design & Construction . . . 12
2.3.2 Method for Measuring the Sound Field . . . 13
2.4 Numerical Simulations . . . 13

3 The Study of Heterogeneous & Hybrid Metamaterials **15**
3.1 Explanation of HG Metamaterial Design . . . 15
3.2 Experimental Results & Discussion . . . 16
3.2.1 Number of Resonators . . . 16
3.2.2 Neck Area of Resonators . . . 17
3.2.3 Multi-Band HG Metamaterials . . . 18
3.2.4 Shape of Resonators . . . 19
3.2.5 Mass of Resonators . . . 21
3.3 Explanation of Hybrid Metamaterial Design . . . 22
3.4 Experimental Results & Discussion . . . 23

4 The Study of Labyrinth Metamaterials **25**
4.1 Explanation of Labyrinth Design . . . 25
4.1.1 Individual Unit Cell Design . . . 25
4.1.2 Prism Design . . . 25
4.2 Experimental Results & Discussion . . . 26
4.2.1 One-Dimensional Impedance Tube . . . 27
4.2.2 Two-Dimensional Waveguide . . . 29

5 Numerical results and discussion **32**
5.1 Hybrid Metamaterials 32
5.1.1 Description of Model 32
5.1.2 Results 33
5.2 Labyrinth Metamaterials 34
5.2.1 Description of Model 34
5.2.2 Results 35

6 Analytical model **39**
6.1 Derivation 39
6.2 Model results 42

7 Conclusions **43**

8 References **46**

List of Figures

1 Example of negative refraction. 1
2 Heterogeneous metamaterial concept. 2
3 Example of a hybrid metamaterial. 4
4 An example of a labyrinth metamaterial structure 5
5 Two-microphone impedance tube for measuring absorption coefficient. 7
6 Four-microphone impedance tube for testing sound transmission loss. 8
7 Standard two-microphone impedance tube schematic. 8
8 Standard four-microphone impedance tube schematic. 9
9 Four-microphone one-dimensional small impedance tube configuration. 10
10 2D waveguide set-up used to perform the sound field mapping. 12
11 Helmholtz resonator and its mass-spring model. 15
12 Helmholtz resonator based HG metamaterial design. 16
13 Effect of changing the number of resonators embedded in the melamine foam. . 17
14 Effect of changing the neck area of the resonators. 18
15 Effect of implementing broadband resonators. 19
16 Resonator design alterations. 19
17 Effect of changing the shape of the resonators. 20
18 Effect of changing the mass of the resonators. 21
19 Schematic of hybrid designs. 22
20 Side view of facesheets. 22
21 Absorption coefficient of hybrid metamaterial with 0.4 mm MPP. 23
22 Absorption coefficient of hybrid metamaterial with 1 mm MPP. 24
23 Labyrinth metamaterial unit cell design. 26
24 Labyrinth metamaterial redesigns. 26
25 CAD Models of assembled prisms. 27
26 Transmission loss of single labyrinth unit cells. 28
27 2D Experiment 1 – 2100 Hz, original structure and unit cells. 29
28 2D Experiment 2 – 2100 Hz, new structure and original unit cells. 30
29 2D Experiment 1 – 2100 Hz, original structure and Redesign 2 unit cells. . . . 30
30 2D Experiment 4 – 1150 Hz, original structure and Redesign 2 unit cells. . . . 31
31 Hybrid metamaterial geometry with the applied physics model sections. 33
32 Mesh convergence study for independent results. 33
33 Thermo-acoustic model results of hybrid metamaterial muffler chambers. . . . 34
34 Schematics of 1D and 2D meshes and convergence for the 1D case. 35
35 Numerical results of prism structure. 35
36 Further numerical results for structure and row interaction. 36
37 Phase variation as the number of units in a 1D row increases. 36
38 Pressure field (a), and mode (b), at 2100 Hz with original units. 37
39 Pressure fields using Redesign 2 units. 38
40 Comparison of transmission angle for original and improved design. 38
41 Schematic representation of a closed-end zig-zag labyrinth. 39
42 Modal introduction in the duct. 42
43 Comparison of Numerical with Analytical results of zig-zag model for $t = 4mm$. 42

List of Abbreviations

HG	Heterogenous
FEM	Finite Element Method
STL	Sound Transmission Loss
H-C	Honeycomb Corrugation
MPP	Micro-Perforated Panel
PHCH	Perforated Honeycomb-Corrugation Hybrid
ASTM	American Society of Testing and Materials
NI	National Instruments
DAS	Data Acquisition System
PA	Pressure Acoustics
PML	Perfectly Matched Layer

1 Introduction

1.1 Introduction to Metamaterials

Metamaterials are defined as macroscopic, composite materials that are engineered to exhibit unusual properties not found in nature. Previously, material properties were determined only by changing the chemical composition of the material. However, recent advancements in techniques such as in 3D printing technology have allowed the macroscopic characteristics of a materials to be easily altered: metamaterials therefore establish their properties from their structural design, rather than their material composition.

Such designs normally consist of multiple individual unit cells — made from conventional materials, such as plastic or metal — that are arranged in repeated formations to make 'crystals' that force waves in a certain direction. These crystals produce sub-wavelength local resonances that can results in the material having extraordinary properties, such as negative effective mass density and bulk modulus – properties that are traditionally strictly positive. When both mass density and bulk modulus (or their electromagnetic counterparts; permittivity and permeability) are negative, a material is said to be 'double negative' or 'left-handed.' A double negative material exhibits negative refractive index, meaning electromagnetic, sound or light waves are refracted in the opposite direction to what would normally be expected (see Figure 1).

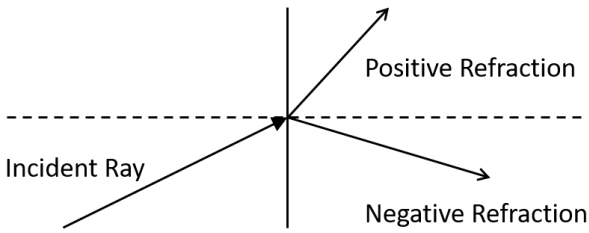

Figure 1: Example of negative refraction.

Metamaterial research spans across multiple disciplines, including fields such as electromagnetism, optics and structural engineering. Acoustic metamaterials especially have attracted significant attention since it was realised that sound waves could be controlled and manipulated in similar ways to how optic metamaterials can control light. Exciting and promising applications of acoustic metamaterials have been realised through recent research, such as the acoustic superlens which can be used in high-resolution clinical ultrasound imaging [1]. Recently, the first three dimensional omni-directional acoustic cloak was created [2] which could be developed to make ships invisible to sonar. Further discoveries include acoustic diodes [3], acoustic "black holes" [4] which can guide sound waves into a core region without scattering, and acoustic metamaterials that exhibit drastically enhanced transmission [5].

Acoustic metamaterials are primarily studied for noise and vibration control, more specifically in the reduction of low frequency noise without the addition of further weight. The manipulation and control of sound waves can be achieved using several different types of repeated structures or 'phononic crystals,' to create a metamaterial. Heterogeneous (HG), hybrid and labyrinth metamaterials are three classes of acoustic metamaterial, whose main functions and example structures are overviewed in Table 1,. Many other combined structures are being

devised that exhibit new or combined properties and behaviour [3]. The aforementioned three classes of metamaterial will be discussed and studied in this report.

Table 1: Classification of metamaterials.

Metamaterial Type	Main function	Example Configurations
Heterogeneous [6]	Absorption of particular frequencies.	Poro-elastic material with periodic mass inclusions. Helmholtz resonator based HG metamaterials. Decorated membrane resonators (DMR).
Hybrid [7]	Broadband absorption at low frequencies.	Honeycombs/ corrugated structures. Perforated panels. Various combinations of the above.
Labyrinth [5]	Manipulate the wave phase, and/or transmission angle.	Maze-like or spiral/coil unit cells. 2D or 3D prismatic arrangement of cells.

1.2 Acoustic Metamaterials

1.2.1 Heterogeneous Metamaterials

Heterogeneous (HG) metamaterials are a class of acoustic metamaterial which have the potential to control a wide frequency range of noise [6]. HG metamaterials consist of a combination of poro-elastic media (such as acoustic foam) and the periodic arrangement of embedded mass inclusions. The combination acts as a mass-spring-damper system as shown in Figure 2. HG metamaterials are designed to exhibit signification noise reduction at the resonant frequency.

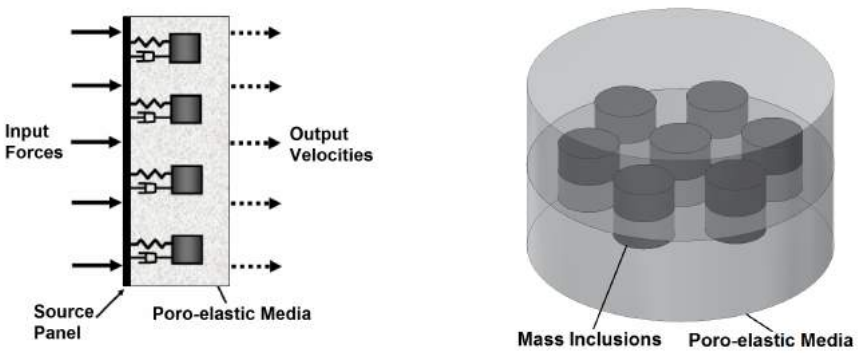

(a) Heterogeneous metamaterial model (Reproduced from [6])

(b) An example

Figure 2: Heterogeneous metamaterial concept.

Several studies have investigated the use of HG metamaterials for noise reduction in different contexts. Groby et al. [8] studied the absorptive properties of simple three-dimensional rigid inclusions embedded in a porous material and verified the results using the Finite Element

Method (FEM). Slagle et al. carried out parametric studies on HG metamaterials experimentally and numerically in order to investigate the factors that affect absorption and transmission loss such as shape, mass and size of embedded inclusions [9]. It was found that the resonant frequency is dependent on the density of embedded masses and the stiffness of the poro-elastic material. Overall, HG metamaterials have relatively high performance for increasing both the sound absorption and sound transmission loss (STL) at low frequencies.

Acoustic foams can be embedded with Helmholtz resonators to create HG metamaterials that can be specifically designed to exhibit high sound absorption at targeted frequencies. The resonant frequency of the system is related to the cavity volume and the neck dimensions. By adjusting these parameters, a particular frequency of sound can be dampened. There are many applications of Helmholtz resonators in engineering, such as acoustic damping in architectural structures [10, 11] or combustion systems [12]. Komkin et al. performed an experimental study using the two-microphone impedance tube method to investigate the absorption coefficient of a Helmholtz resonator [13]. It was found that the main cause for sound absorption – viscous loss – is proportional to the resonator neck diameter and weakly depends on the neck length or cavity depth. Another experimental study by Romadhona et al. [11] found that low frequency sound absorption of a wooden sound diffuser element could be significantly improved by adding Helmholtz resonator inclusions. Groby et al. [14] also found that embedding Helmholtz resonators into a hard-backed porous material improved the sound absorption at the resonant frequency and higher frequencies due to the excitation of a trapped mode. It is now important to study how Helmholtz resonator HG metamaterials can be optimised to aid the development of thin and lightweight metamaterials with high sound absorption.

1.2.2 Hybrid Metamaterials

Hybrid acoustic metamaterials are a new class of sub-wavelength metamaterials that have the ability to possess broadband absorption at low frequencies. They are similar to HG metamaterialsas as they make us of resonators to dampen sound, but without the need for a poro-elastic frame.

Nia et al. [15] constructed an aluminium metamaterial with a hexagonal cell honeycomb structure, and studied the effects of foam filling the honeycombs. Compared to the empty honeycombs, it was found that the specific absorbed energy (SAE) and specific structural strength of honeycombs was increased. The existence of foam in panels increases the energy absorption capacity by increasing the number of 'folds' in the material. Cote et al. [16] manufactured a metamaterial using corrugated and diamond lattice sandwich panels. Like the honeycombs, the corrugations were found to have high specific stiffness and strength. However, the corrugated structure also had a lower energy absorption capacity.

Inspired by these studies, Han et al. [17, 18] proposed to combine honeycombs with corrugations and construct a honeycomb-corrugation (H-C) hybrid sandwich core. The strength and energy absorption of a hybrid sandwich core is enhanced when these two techniques are combined. Tang et al. [7] further developed this to create a metamaterial with micro-perforated panels (MPP) on top of the H-C core. The structure is shown in Figure 3. These MPP panels are formed of individual Helmholtz resonators with sub-millimeter hole diameter [19]. The perforated H-C hybrid exhibits super broadband low-frequency sound absorption. Tang et al. found that using a smaller hole diameter and thicker facesheet provided the highest absorption at lowest frequency.

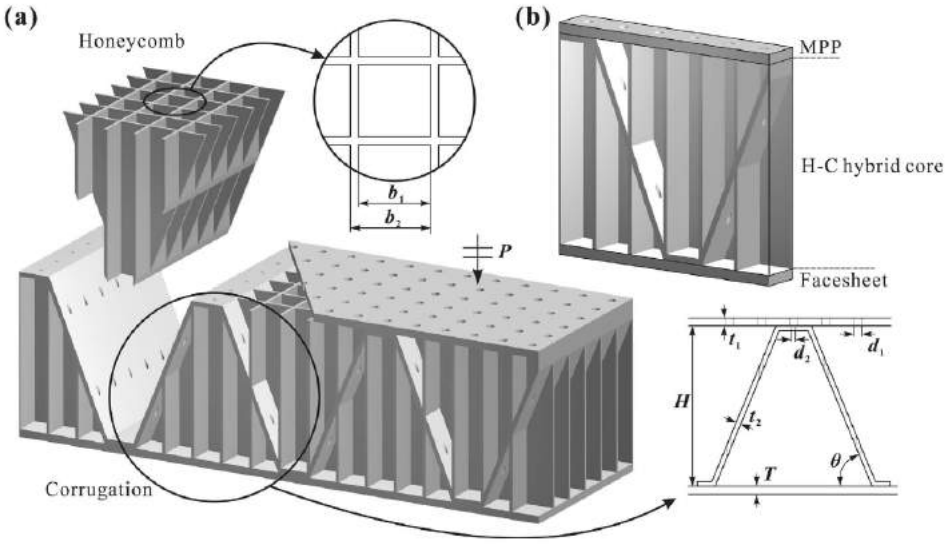

Figure 3: Example of (a) a PHCH metamaterial made up of (b) unit cells of MPP and honeycomb-corrugation hybrid core. (Reproduced from [7]).

1.2.3 Labyrinth Metamaterials

Another extraordinary property that metamaterials can possess is negative refractive index, but materials with such a property cannot be found in nature. In addition to this, the Helmholtz resonator based metamaterials mentioned in Section 1.2.1 can only produce high sound absorption across a narrow band gap. The ability to create a material that possesses both broadband sound attenuation and negative refractive index could result in many exciting applications. An example of such an application would be in aeroplanes, where a much more comfortable customer experience could be provided if low frequency engine noise could be attenuated but also redirected away from the passengers into the sky above.

Such materials have been realised in the form of labyrinth metamaterials, an example of which is shown in Figure 4. As the name suggests, these are formed of small, maze-like structures with sub-wavelength slits [20] and have the ability to possess double negativity [5, 20, 21] and a variety of transmission characteristics. Liang et al. [5] first proposed a labyrinth metamaterial design with zig-zag type channels. The labyrinth structure works by providing the propagating perturbation with an alternate, extended route through folded, narrow channels [5], acting as a space-coil. The speed of the effective fluid particles in the labyrinth is therefore ultra-slow [22]. This macroscopically appears to delay the phase of the wave relative to its initial path [23]. By combining multiple labyrinth unit cells into specific array configurations, the phase at each row exit can be adjusted to control the transmission angle of the transmitted wave, and even produce negative refraction.

The dimensions of the labyrinth units can be edited to provide a specific phase difference. Liang et al. used a variation of their original configuration to design a metamaterial with low absorption and extreme dispersion including conical dispersion for airborne sound at low frequencies [24]. Frenzel et al. [23] use the design to fabricate a three-dimensional metastructure which achieves broadband sound attenuation. Xie et al.[21] experimentally demonstrated that this labyrinth design has a negative refractive index across a broad frequency range. Such geometries can also be used to transfer a plane wave through a constriction (such as a corner in a pipe), whilst maintaining the initial wave form that was present at the constriction entrance

[5, 22, 25, 26]. This phenomena is called sound tunnelling and can also be achieved by homogeneous membranes that have a similar effect [27].

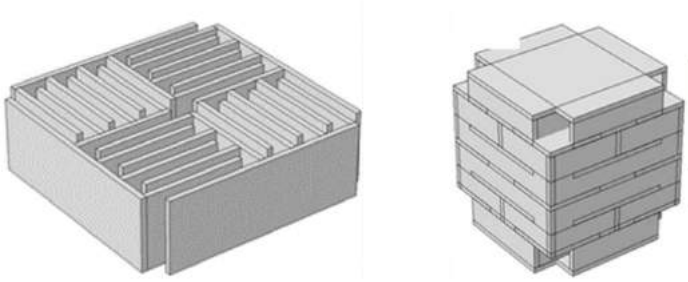

(a) 2D Maze (b) 3D Space Coiling

Figure 4: An example of a labyrinth metamaterial structure (Reproduced from [28]).

Spiral geometrical shapes aim to manipulate the phase gradient under the same principles but using only 1D unit rows, since the coiling of a spiral can be increased locally, resulting in a more condensed increase of the wave path [29, 30]. The above geometries have also been tested in other types of application including focusing, beam steering and conversions from cylindrical to plane waves [22, 25, 31]. Combinations of both labyrinth and spiral unit types have also been tested and simulated to produce asymmetric transmission relative to the incident wave [32].

The existing studies on labyrinth metamaterials are mostly based on experimental and numerical work although there have been some attempts for the analytical formulation of a single path zig-zag labyrinth with reflection [31]. However, due to the complexity of the calculations there are multiple errors which produce non-reasonable results (for example, any even power of M_1 (Equation (13)) gives the identity matrix). The current study will attempt to produce the correct expressions of this problem in Section 6.

1.3 Objectives

Research into acoustic metamaterials has witnessed astonishing development over the last decade. Such developments have the potential to offer new, interesting methods for sound control and manipulation, which will lead to exciting applications across a wide range of industries. However, since the field of acoustic metamaterials is a relatively new and broad area of study, there is still much more that needs to be understood before such applications can be realised.

Therefore, the aim of this research is to study acoustic metamaterials in different contexts in order to better understand their underlying physics. Heterogeneous (HG), hybrid and labyrinth metamaterials will be studied using experimental, numerical and analytical techniques. The main objectives for this study are described below.

Heterogeneous and Hybrid Metamaterials:

- Perform experiments inspired by Slagle et al. [9] and Groby et al. [14], on Helmholtz resonator based HG metamaterials to study how varying their geometric parameters affects absorption and sound transmission loss (STL).
- Design a hybrid acoustic metamaterial based on the work of Tang et al. [7] with the aim of achieving broadband low frequency sound attenuation.

Labyrinth Metamaterials:

- Design and construct a one-dimensional (1D), square section impedance tube to study the STL of four different labyrinth designs, with the aim of achieving low frequency, high transmission losses.
- Replicate an experiment performed by Xie et al. [21] to demonstrate that negative refraction can be achieved through a prism comprised of 55 unit cells. This involves designing a two-dimensional (2D) waveguide method which can measure the spatial variation of the sound field after the prism structure.
- Investigate how small and large scale design changes on the prism affect the refraction angle.

Numerical & Analytical Modelling:

- Use COMSOL software to simulate the acoustic behavior and absorption coefficient of the redesigned hybrid metamaterial based on the method used by Tang et al. [7], and to compare with our experimental results.
- Replicate the extraordinary negative index results of Xie et al. numerically. Furthermore, perform numerical simulations of 1D and 2D labyrinth cases to improve the understanding of their transmission mechanism.
- Maintain communication between numerical and experimental results to assess and validate their accuracy, and to further explore the capabilities of labyrinth metamaterials.
- Develop an analytical model to describe and calculate the space-coiling acoustic performance of closed-end zig-zag units.

2 Experimental & Numerical Methods

The three experimental set-ups used in this study will be described in this section, followed by the background physics of the numerical work.

2.1 Circular Section Impedance Tube

The impedance tube method is a convenient way to measure acoustic properties such as absorption coefficient and normal incident transmission loss using two or four microphones respectively. Plane waves are generated inside the tube using a speaker and the sound pressure is measured simultaneously at each microphone location. This can be decomposed into forward- and back-travelling components to retrieve the full transfer matrix through the sample. Calculations can then be performed to retrieve important acoustic properties such as absorption coefficient and sound transmission loss (STL).

The circular section impedance tube was manufactured by Lee et al. [33] according to the American Society of Testing and Materials (ASTM) standard test methods E1050 - 12 [34] and E2611 - 17 [35]. Specimens can be tested in the frequency range 250-2000 Hz. This impedance tube is used to measure the absorption coefficient and STL for the heterogeneous (HG) and hybrid metamaterials.

2.1.1 Two Microphone Set-up

The two microphone set-up (Figure 5) can be used to measure the sound absorption coefficient. A broadband, 'white noise,' signal is produced by a signal generator, passed through an amplifier and then a speaker. The amplifier and two microphones are connected to different channels of the National Instruments (NI) Data Acquisition System (DAS), then through to a computer. The test specimen is inserted in the left end of the tube and a backing plate is applied using nuts and bolts. Finally, the data collected by the DAS is analysed in MATLAB.

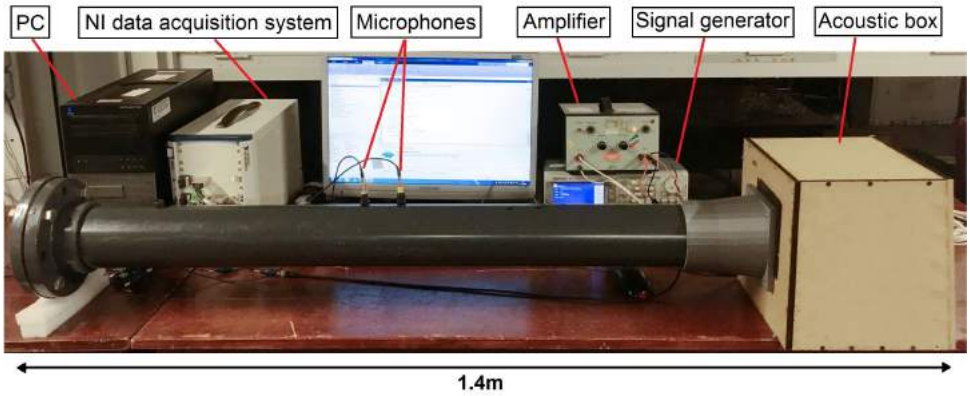

Figure 5: Two-microphone impedance tube for measuring absorption coefficient.

2.1.2 Four Microphone Set-up

The four microphone impedance tube setup (Figure 6) can be used to measure STL. The backing plate is removed and another section of tube is mounted to the previous one by flanges, nuts and bolts. Two more microphones are mounted to this section of tube and connected to the DAS.

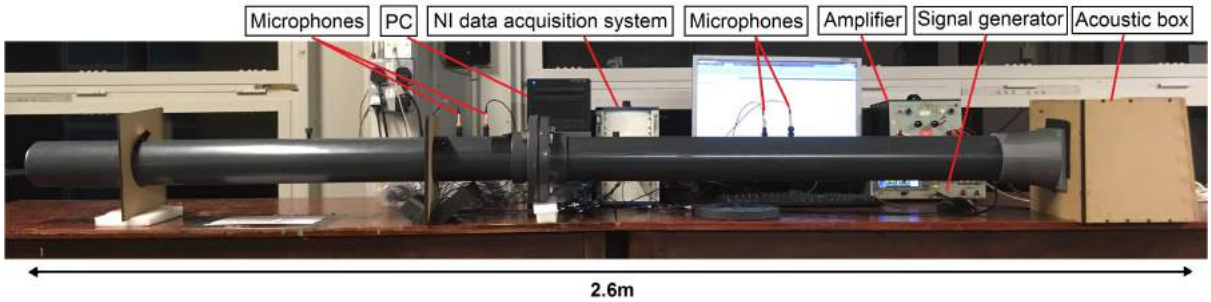

Figure 6: Four-microphone impedance tube for testing sound transmission loss.

2.1.3 Impedance Tube Measurement Methods

As described in Sections 2.1.2 and 2.1.1, two different measurement methods are used to retrieve the absorption coefficient and STL. The following section describes how these parameters are extracted from the collected signals.

Normal Incidence Sound Absorption Coefficient

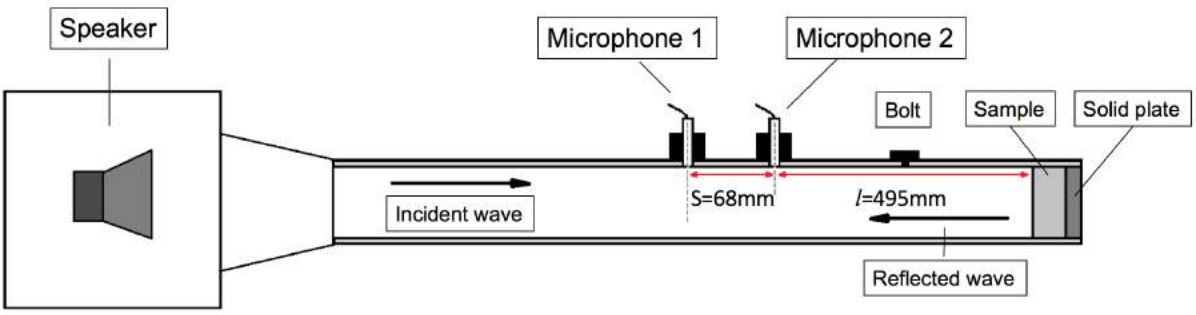

Figure 7: Standard two-microphone impedance tube schematic.

The transfer function (H) is calculated by taking the complex ratio of the Fourier transforms between the acoustic pressure at the microphone 1 (G1) and microphone 2 (G2):

$$H = \frac{G_1}{G_2}. \tag{1}$$

Then, Equation 1 can be used to calculate complex reflection coefficient (R):

$$R = \frac{H - e^{-jks}}{e^{jks} - H} e^{j2k(l+s)}, \tag{2}$$

where c is speed of sound and k is wavenumber. The normal incidence sound absorption coefficient α is computed using:

$$\alpha = 1 - |R|^2. \tag{3}$$

Normal Incidence Transmission Loss

The schematic of the standard four-microphone impedance tube configuration is shown in Figure 8.

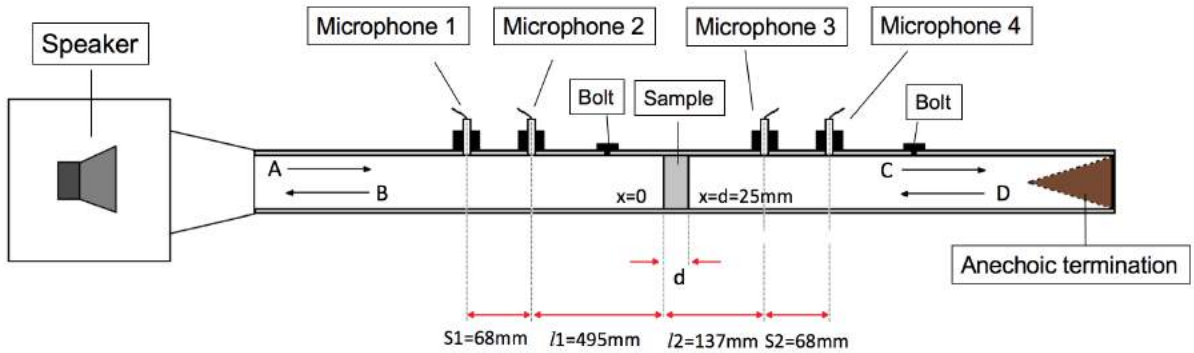

Figure 8: Standard four-microphone impedance tube schematic.

This method finds STL by using terms from the transfer matrix that relate the acoustic pressure and particle velocity on the front and back surface of the specimen using Equations 4, 5 and 6. Two different terminations are involved: anechoic (o) and blocked (c):

$$\begin{bmatrix} p_o \\ u_o \end{bmatrix}_{x=0} = \begin{bmatrix} T_{11} & T_{12} \\ T_{21} & T_{22} \end{bmatrix} \begin{bmatrix} p_o \\ u_o \end{bmatrix}_{x=d}, \tag{4}$$

$$\begin{bmatrix} p_c \\ u_c \end{bmatrix}_{x=0} = \begin{bmatrix} T_{11} & T_{12} \\ T_{21} & T_{22} \end{bmatrix} \begin{bmatrix} p_c \\ u_c \end{bmatrix}_{x=d}. \tag{5}$$

$$\begin{bmatrix} T_{11} & T_{12} \\ T_{21} & T_{22} \end{bmatrix} = \begin{bmatrix} \frac{p_{0o}u_{dc}-p_{0c}u_{do}}{p_{do}u_{dc}-p_{dc}u_{do}} & \frac{p_{0c}p_{do}-p_{0o}p_{dc}}{p_{do}u_{dc}-p_{dc}u_{do}} \\ \frac{u_{0o}u_{dc}-u_{0c}u_{do}}{p_{do}u_{dc}-p_{dc}u_{do}} & \frac{p_{do}u_{0b}-p_{dc}u_{0o}}{p_{do}u_{dc}-p_{dc}u_{do}}. \end{bmatrix} \tag{6}$$

To populate this transfer matrix, the pressure and wave velocity before and after the sample are found:

$$p_o = A + B \tag{7}$$

$$p_d = Ce^{-jkd} + De^{jkd} \tag{8}$$

$$u_o = \frac{A-B}{c\rho} \tag{9}$$

$$u_d = \frac{Ce^{-jkd} - De^{jkd}}{c\rho} \tag{10}$$

using:

$$A_{ref} = j\frac{H_{1,ref}e^{-jkl_1} - H_{2,ref}e^{-jk(l_1+s_1)}}{2sinks_1} \tag{11}$$

$$B_{ref} = j\frac{H_{2,ref}e^{jk(l_1+s_1)} - H_{1,ref}e^{jkl_1}}{2sinks_1} \tag{12}$$

$$C_{ref} = j\frac{H_{3,ref}e^{jk(l_2+s_2)} - H_{4,ref}e^{jkl_2}}{2sinks_2} \tag{13}$$

$$D_{ref} = j\frac{H_{4,ref}e^{-jkl_2} - H_{3,ref}e^{-jk(l_2+s_2)}}{2sinks_2} \tag{14}$$

Sound transmission coefficient, τ, is the ratio of sound power that is transmitted and radiated on the other side of specimen to sound power incident on a material. The equation is derived as:

$$\tau = \frac{2e^{jkd}}{T_{11} + (\frac{T_{12}}{c\rho}) + c\rho T_{21} + T_{22}} \tag{15}$$

Sound transmission loss, STL, is defined as ten times the common logarithm of the reciprocal of the sound transmission coefficient.

$$TL = 10log_{10}\left|\frac{1}{\tau}\right| \tag{16}$$

The results of experiments carried out using this set-up can be seen in Section 3.2 and 3.4.

2.2 Square Section Impedance Tube

A 1D impedance tube was specially designed and constructed by us to measure the STL across labyrinth unit cells. The set-up of the impedance tube can be seen in Figure 9. The tube consists of two long Perspex sections with constant, square cross-section and a separate specimen holder of the same cross-section, which are connected together. The impedance tube was designed such that one unit cell (26 mm^3) filled the entire square section of the tube. Other than the cross sectional shape and dimensions, this tube follows the same set up as the circular section impedance tube. The same method was used to collect and process reflection and transmission coefficients as described in Section 2.1.3. The results of experiments carried out using this set-up can be seen in Section 4.2.1.

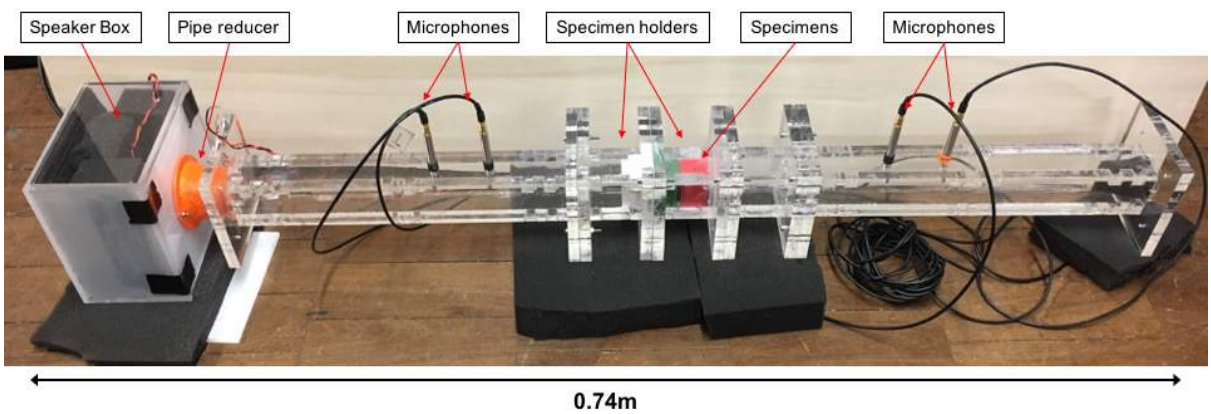

Figure 9: Four-microphone one-dimensional small impedance tube configuration.

2.2.1 Design & Construction

The impedance tube was designed and constructed in relation to the E2611-17 Standard [35]. Important parameters that must be considered include; microphone spacing, the specimen holder, calibration of microphones and specifications of the microphones and speaker. Details of these are described below.

Microphone Positioning: The frequency range of interest for the experiment was below 3000 Hz. The microphone positioning and spacing can therefore be calculated using equations presented in the standards. The standards state that the maximum microphone spacing, s, must be no larger than 80% of the shortest half wavelength of interest (f_u=3000 Hz),

$$s \ll \frac{0.8c}{2f_u}, \tag{17}$$

where c is the speed of sound. This equates to 45.7 mm. A large spacing between microphones increases the accuracy of the measurements, so a microphone spacing of 40 mm was chosen. As the speaker generates non-plane waves as well as plane waves, the length between the speaker and the first microphone must be of sufficient length to allow the non-plane waves to diminish and the plane waves to fully develop. The standard suggests a minimum distance of three tube diameters between the speaker and first microphone,

$$3d \ll a, \tag{18}$$

which is 78 mm. This distance was chosen to be 200 mm. The standards state that the distance between the second microphone and the sample is dependent on the surface characteristics of the test sample. As the metamaterial unit cell is an asymmetric surface, the second microphone should be at least two tube diameters from the sample, which equates to at least 52 mm. This dimension was therefore chosen to be 80 mm. This allows for the dissipation of higher order modes which result from rough surfaces.

Microphones: Four 7 mm G.R.A.S. microphones were used in all experiments. Rubber stoppers were used to control the depth of the microphones in the microphone ports to ensure their diaphragms were flush with the inside surface of the tube.

Specimen Holder: A detachable specimen holder was constructed out of Perspex with identical internal dimensions to the tubes. The metamaterial unit cells can be slotted into the holder. It must be ensured that there is minimal space around the edge to reduce the effect on the transmission loss calculations. The design of the specimen holder allows the metamaterial samples to be changed with ease.

Speaker and Acoustic Box: A 5 cm circular diameter Visaton FRS 5 loudspeaker (frequency response 150 Hz-20 kHz) was connected to the 26 mm square diameter impedance tube using a 3D printed pipe reducer. The standards required that the speaker must be sealed and isolated from the impedance tube to minimise structure-borne sound excitation of the tube [35]. Therefore, an acoustic box was manufactured to contain the loudspeaker. This was lined with acoustic foams to prevent leakage and internal sound reflections. The acoustic foam on the back wall of the box was inclined to prevent standing waves from forming.

Calibration: The transfer function method described in the standards was used to calibrate the microphones. This involved switching each microphone into position one in turn and measuring the correction transfer function. This allowed the microphone amplitude and phase differences to be normalised to the first microphone, which is used as a reference signal.

Additional Information After taking initial readings, it was clear that some frequency bands were setting up standing waves in the tube which had nodes at microphone 3. Extra tube length was therefore added between the specimen holder and second tube in order to removes these nodes.

2.3 Two-Dimensional Waveguide

A 2D waveguide was designed and constructed by us to replicate the experimental set-up used by Xie et al. [21, 36]. The waveguide is used to replicate the findings produced by Xie et al which proves that a labyrinthine unit cell prism structure possesses a negative refractive index.

2.3.1 Design & Construction

Two parallel 5 mm ABS plastic plates were positioned 50.8 mm apart using adjustable spacers. This separation distance results in an upper cut-off frequency of 3.38 kHz, which is above the highest frequency of interest. Between the plates, three identical speakers were placed at one end of a smaller, rectangular source waveguide. The sound hard boundaries of this Perspex waveguide allow waves to become planar before reaching the prism structure, located on the other end of the source waveguide. The outer perimeter of the ABS sheets were covered by acoustic foam to minimise reflection. 14 microphones placed at 14 mm apart were mounted on a traverse system in the measuring area. The set-up can be seen in Figure 10.

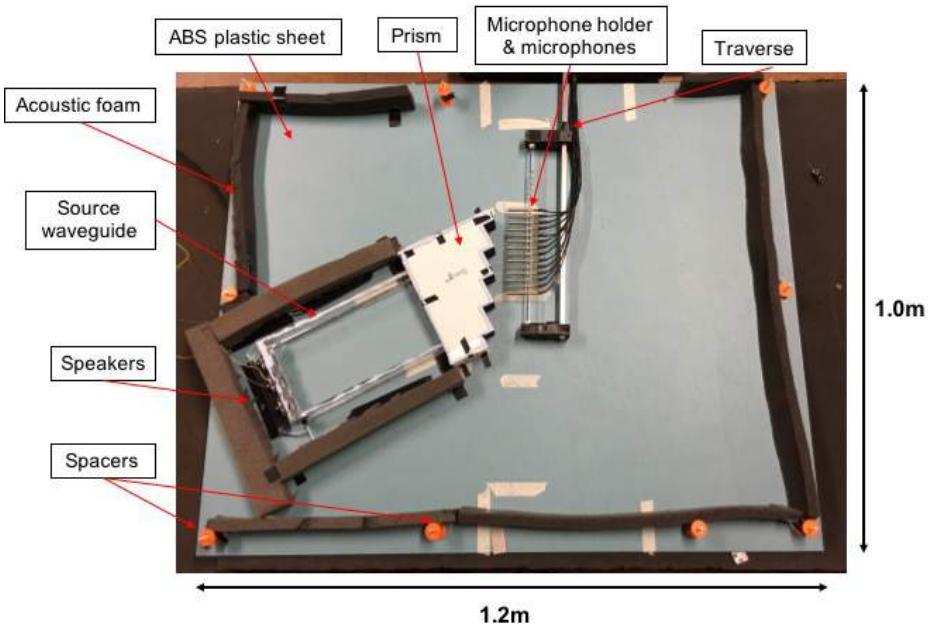

Figure 10: 2D waveguide set-up used to perform the sound field mapping.

2.3.2 Method for Measuring the Sound Field

A signal generator was used to produce a tone at the frequency of interest. The signal exiting the prism was then detected by the microphones in a 0.7x0.3 m measuring area. Note, Xie et al. [21] stated that microphone data was taken every 20 mm in their method, but it was decided to increase the number of measuring points in order to improve resolution. The traverse was moved in steps of 10 mm and microphone signals were collected using an NI DAS. This resulted in a grid of 31x56 data points in the measuring area. Sensitivity values for the microphones (taken using a pistonphone) were used to convert the microphone signals from Volts to Pascals. The root mean squared pressure was then calculated for each point. The pressure field from four separate sweeps were combined to produce the total acoustic field for the measuring area. The results of experiments carried out using this set-up can be seen in Section 4.2.2.

2.4 Numerical Simulations

This section will discuss the background physics used in the numerical simulations throughout this report.

The Finite Element Method (FEM) analysis in acoustics involves the numerical solution of linear expressions. These approximate the analytical, non-linear partial differential equations of particle pressure in a sound wave. COMSOL is commonly used for acoustic simulations of any kind and was therefore used for computational analysis. The variation of the pressure profile of the propagating acoustic waves was investigated by solving the field of the contained fluid (air) for each geometry. The Helmholtz equation was solved by applying the Pressure Acoustics (PA) model assuming a line source, Q_m, given by:

$$\nabla \cdot \Big(-\frac{1}{\rho_c}(\nabla p_t - q_d)\Big) - \frac{k_{eq}^2 p_t}{\rho_c} = Q_m, \tag{19}$$

where

$$p_t = p + p_b, \tag{20}$$

$$k_{eq}{}^2 = \left(\frac{\omega^2}{c_c}\right) - k_z{}^2, \tag{21}$$

$$c_c = c, \quad \rho_c = \rho, \tag{22}$$

and p_t is the sum of the sound pressure, p, and the background acoustic pressure, p_b, k_{eq} is the wavenumber along the direction of the wave, k_z is the out of plane wavenumber, ω is the natural frequency and ρ is the material density.

In acoustic metamaterials, high STL is a property of high interest because it provides soundproofing properties [37]. The expression of STL is given by:

$$STL = 10\log_{10}\left(\frac{W_{in}}{W_{out}}\right), \tag{23}$$

where W_{in} and W_{out} is the power of the incoming and the outgoing sound wave respectively given by:

$$W_{out} = \int_{\partial\Omega} \frac{p^2}{2\rho_c c_c} dA, \tag{24}$$

$$W_{in} = \int_{\partial\Omega} \frac{{p_o}^2}{2\rho_c c_c} dA. \tag{25}$$

Since we are dealing with a big range of eigenfrequencies, the expected results also have wide variations between them. Thus, the initial value of pressure at 1 Pa across the geometry was selected since the computational time was not considerably affected. Furthermore, the application of the following 3 basic boundary conditions [38] was necessary in order to obtain reliable results in all the simulated geometries.

1) Plane wave radiation on inlet and outlet boundaries in order to allow waves to propagate in and out of the simulated geometry. The expression of the pressure, is given by:

$$-n \cdot \Big(-\frac{1}{\rho_c}(\nabla p_t - q_d)\Big) + i\frac{k}{\rho_c} p + \frac{i}{2k\rho_c}\Delta_T p = Q_i, \tag{26}$$

where

$$Q_i = i\frac{k}{\rho_c} p_i + \frac{i}{2k\rho_c}\Delta_T p_i + n \cdot \frac{1}{\rho_c}\nabla p_i, \tag{27}$$

and p_i the incident pressure field.

2) Hard wall boundary, which assumes that the particle velocity will be zero on the wall boundaries, given by:

$$-n \cdot \Big(-\frac{1}{\rho_c}(\nabla p_t - q_d)\Big) = 0, \tag{28}$$

where n is the unit vector normal to the wall boundary.

3) Perfectly Matched Layer tramsformation acts as an artificial absorbing layer, which changes the value of $\theta/\theta x$ at the boundary, thus gradually attenuating the pressure of the wave:

$$\frac{\theta}{\theta x} \rightarrow \frac{1}{1+\frac{i\sigma(x)}{\omega}} \frac{\theta}{\theta x}, \tag{29}$$

where ω is the angular frequency and σ is a function of x. When $\sigma > 0$, the propagated waves are attenuated. The application of the above model will be discussed in Section 5 for all the studied geometries.

3 The Study of Heterogeneous & Hybrid Metamaterials

This section will present several experiments on Helmholtz resonator based HG metamaterials, which involve investigating how changing various parameters affect the sound attenuation of the sample. Geometric parameters include changing the number of resonators, neck area and shape. An attempt to achieve broadband sound attenuation is also presented by developing a basic multi-band metamaterial. Changing the mass of the resonators is also studied. A hybrid metamaterial is then designed, inspired by Tang et al. [7], and its absorption characteristics are studied.

3.1 Explanation of HG Metamaterial Design

The HG metamaterial proposed by Groby et al. [14] combines the effect of Helmholtz resonator inclusions and poro-elastic material. This results in high sound absorption particularly at the resonator's resonant frequency. A Helmholtz resonator is a solid shell containing a cavity of air with a small neck opening (Figure 11). It can be thought of as a mass-spring system, with the volume of air in the neck and the cavity of air acting as a lumped mass and the spring respectively. Sound pressure applied to the resonator causes the mass to oscillate, resulting in the cavity of air being compressed and expanded. This results in energy dissipation at the resonant frequency [39].

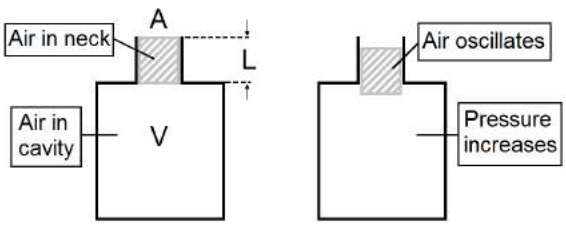

Figure 11: Helmholtz resonator and its mass-spring model.

The resonant frequency f is given by:

$$f = \frac{c}{2\pi}\sqrt{\frac{A}{VL_{eff}}}, \tag{30}$$

where c is the sound velocity, A is the neck area, V is the cavity volume and L_{eff} is the effective length of the neck [40]. The effective neck length is slightly larger than the physical neck length because, in a real resonator, the air in the neck oscillates over a distance greater than the physical neck length. A correction is therefore added to the neck length and is computed as:

$$L_{eff} = L + 0.6R + \frac{8}{3\pi}R, \tag{31}$$

where L is the physical length of the neck and R is the radius of the neck.

The Helmholtz resonators were fabricated using a 3D printer and embedded into 25 mm thick melamine foam with a diameter of 99 mm. The dimensions of resonator and a sample of one of the HG metamaterials are shown in Figure 12. All tests were performed in the circular impedance tube mentioned in Section 2.1.

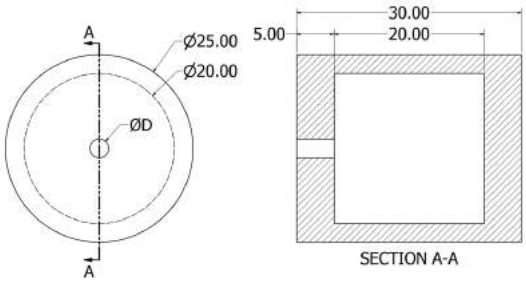

(a) Resonator dimensions

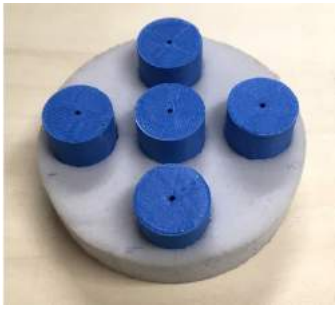

(b) HG material

Figure 12: Helmholtz resonator based HG metamaterial design.

3.2 Experimental Results & Discussion

3.2.1 Number of Resonators

First, the effect of varying the number of resonators embedded in the foam was studied. Tests were performed on HG metamaterials with three, five and seven identical resonators. All resonators had a 2.5 mm neck diameter. A baseline test using the foam with no mass inclusions was also performed. The results of absorption coefficient and STL are shown in Figure 13. Results for an empty tube are also shown on this graph – the absorption coefficient should theoretically be zero, as all the sound should be reflected. It can be seen that the experimental result has a very low value overall, but it is not equal to zero. This is due to leakage in the tube. The absorption coefficient of melamine foam is relatively small at low frequencies, gradually becoming larger with increasing frequency.

The resonant frequency of the resonators can be calculated using Equation 30 as 585 Hz. The peaks in absorption coefficient for all three sets of resonators are found between 570-580 Hz, which is very close to the theoretical frequency. The slight discrepancy between the experimental and theoretical values could be due to the estimation of L_{eff}. It can be concluded that there is a clear increase in absorption coefficient at the resonant frequency as the number of resonators increases. The seven resonator sample shows an substantial increase in absorption coefficient across a broad frequency range (600-1600 Hz). This behaviour agrees well with findings by Groby et al. [14] who suggested the presence of a trapped mode between the back of the resonators and the backing plate. At resonant frequencies, sound will be trapped in this space until it is dissipated into heat. More energy is trapped as the surface area of the resonators increases with increasing number.

As for STL, the empty impedance tube line is very close but not equal to 0 dB for the most part, as would be expected, due to small viscous losses along the tube. With only foam inside the tube, the STL increases but with a clear dip at 440 Hz. This behaviour is in perfect agreement with the results foud by Slagle et al. [9] and Lee et al. [33] both experimentally and numerically. The three resonator metamaterial is not able to remove the dip caused by melamine foam. Instead, the dip is reduced by 1 dB and shifted to 770 Hz. The seven resonator sample not only removes the dip, but also dramatically increases the STL between 300 Hz and 1600 Hz. For all three samples, a peak can be seen at the resonant frequency.

Overall, it has been found that the number of resonators has significant effects on sound absorption coefficient and STL of the HG metamaterial. However, it must be noted that increasing the number of resonators also increases the mass of the metamaterial which is not desirable.

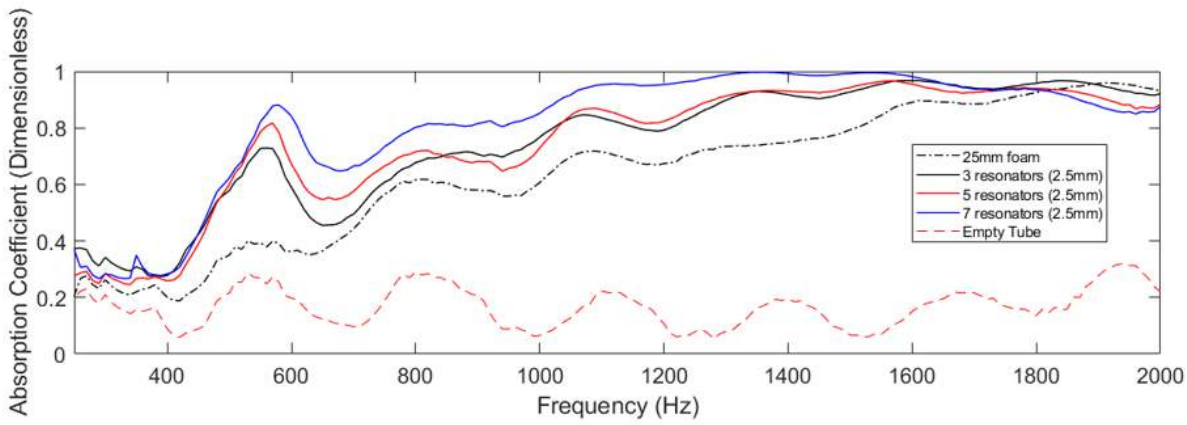

(a) Absorption Coefficient

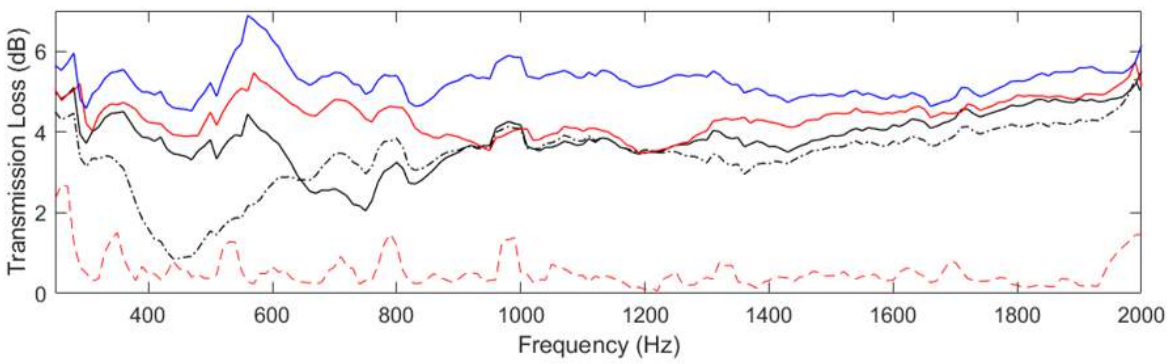

(b) Transmission Loss

Figure 13: Effect of changing the number of resonators embedded in the melamine foam.

3.2.2 Neck Area of Resonators

Equation 30 can be used to fine tune the Helmholtz resonator's geometric parameters to target a specific frequency. Komkin et al. found that sound absorption strongly depends on the resonator neck area rather than the neck length or cavity depth [13]. This means the resonant frequency can be changed most effectively without increasing the thickness of the metamaterial, as would be desired. As a result, two more metamaterial samples were designed with 2 and 3 mm neck diameters, and compared to the previous results for $D = 2.5$ mm. Five resonators were used in all samples. The results can be seen in Figure 14.

The resonant frequency of 2 mm and 3 mm resonators can be calculated as 481 Hz and 684 Hz respectively. The experimental results are in almost perfect agreement, with peaks at 480 Hz and 690 Hz. The absorption coefficients of all samples have exceeded 0.8, confirming that this type of HG metamaterial can be easily designed to exhibit high absorption at targeted frequencies. This gives rise to the possibility that by combining resonators with different neck areas, broadband sound absorption could be sort. This hypothesis is tested and discussed in Section 3.2.3.

The STL of all three samples are very similar to each other: again, the dip at 440Hz is eliminated for all three metamaterials and improvements are seen between 300 Hz and 800 Hz. As all sets of resonators have reduced the dip by very similar amounts, it is concluded that STL is more likely affected by the size of the embedded inclusions and not the neck area. Near its resonant frequency, only the 3 mm resonator sample has a noticeable effect which is about 2 dB

more than other samples. Apart from this, the resonators have little affect on the STL compared to the melamine foam alone.

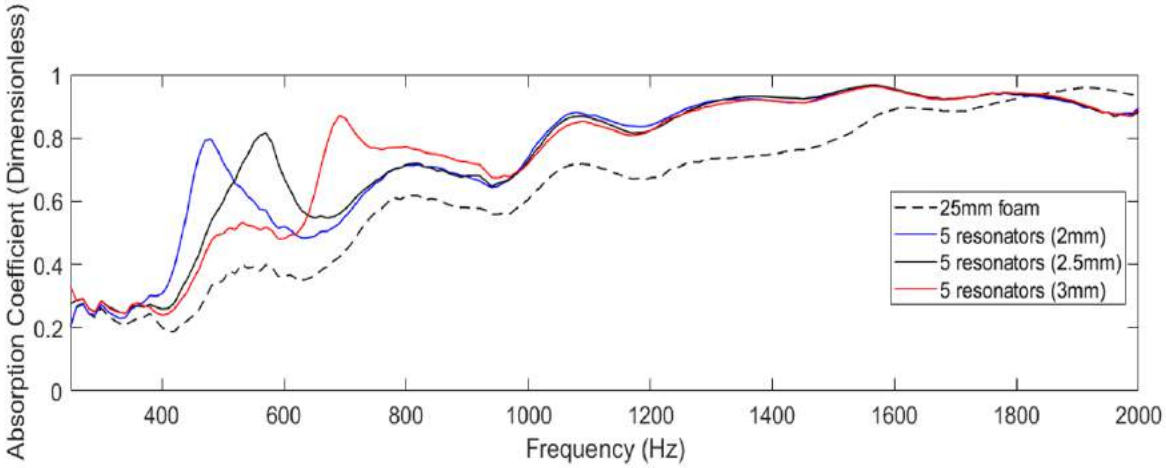

(a) Absorption Coefficient

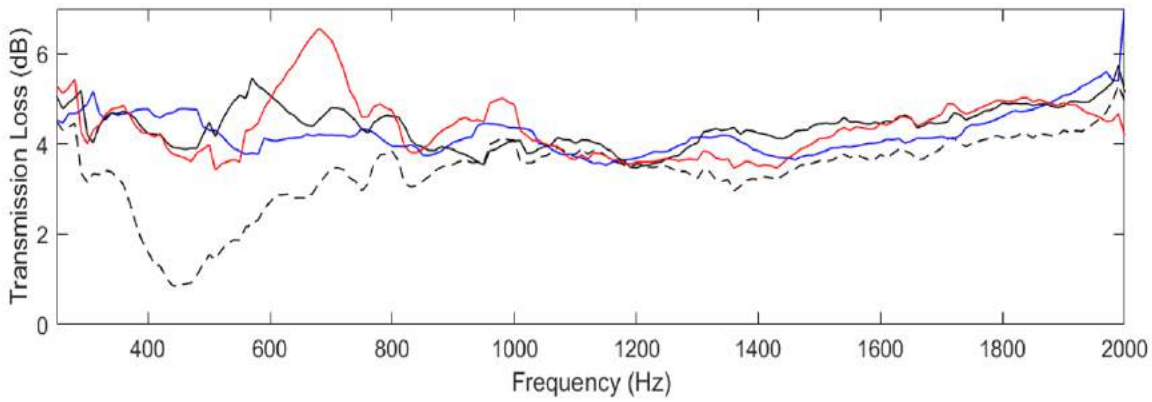

(b) Transmission Loss

Figure 14: Effect of changing the neck area of the resonators.

3.2.3 Multi-Band HG Metamaterials

Previous tests found that the HG metamaterials were successful at increasing absorption coefficient and STL at the resonant frequency. However, there are circumstances where high sound attenuation across a broad frequency range might be desired. To try and achieve this, a combination of three 2 mm and two 3 mm Helmholtz resonators were embedded into some foam. These results are compared to the those previously found in Section 3.2.2 and are shown in Figure 15 by the solid black line.

It can be seen that peaks in absorption coefficient have now been achieved at both resonant frequencies. The values for absorption coefficient are slightly reduced, as would be expected, as less resonators of each type are used. The dip between the two peaks could be removed by using resonators with resonant frequencies closer together. There is little effect on the STL for reasons discussed previously. These results promisingly show that by using combinations of different resonators, HG metamaterials can easily be designed to exhibit broadband sound attenuation across a desired frequency range.

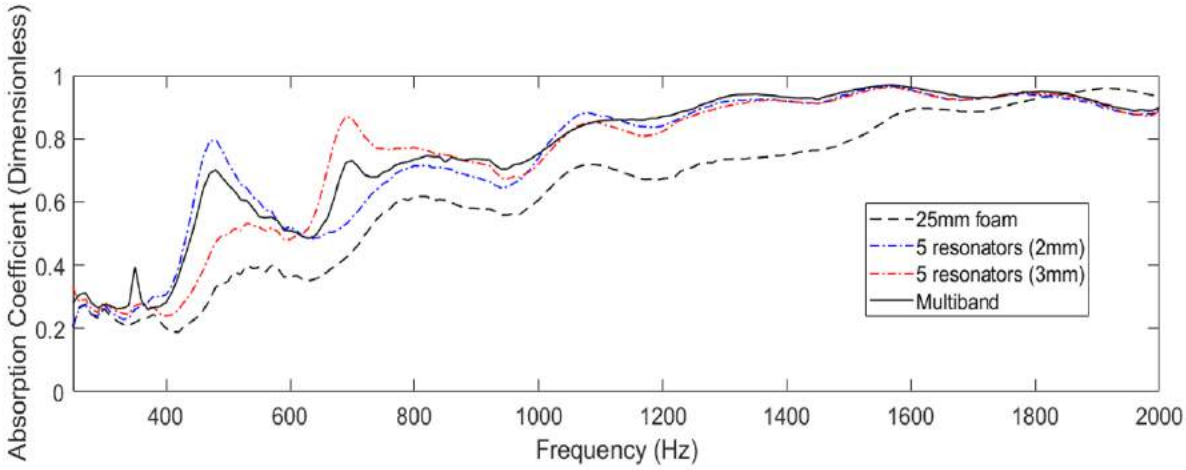

(a) Absorption Coefficient

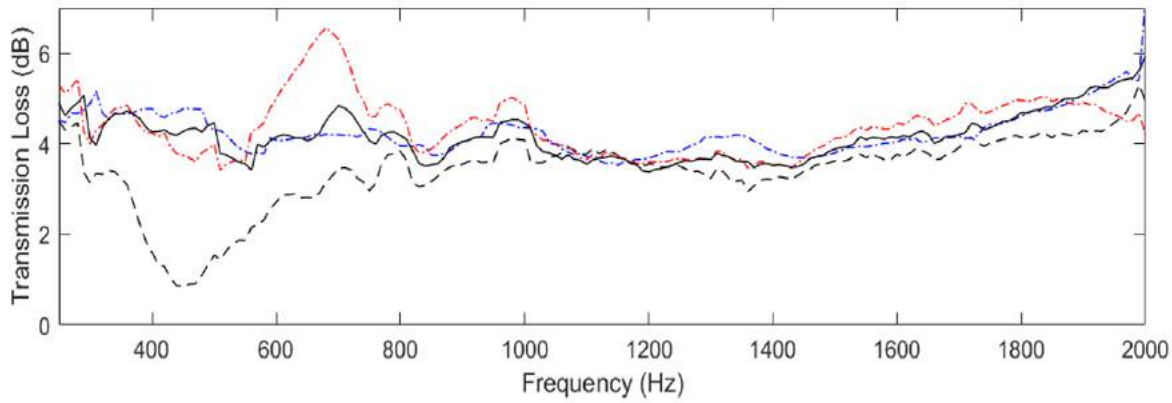

(b) Transmission Loss

Figure 15: Effect of implementing broadband resonators.

3.2.4 Shape of Resonators

All the changes made so far have been found to have little effect on the STL. It was propositioned that changing the shape of the resonator could potentially provide some variation in this. Therefore, two further Helmholtz resonators were designed: Design A remains cylindrical but has a protruding neck of 5 mm, while the shape of the Design B is changed to a cuboid. Drawings of the resonators and the test results are given in Figures 16 and 17 respectively.

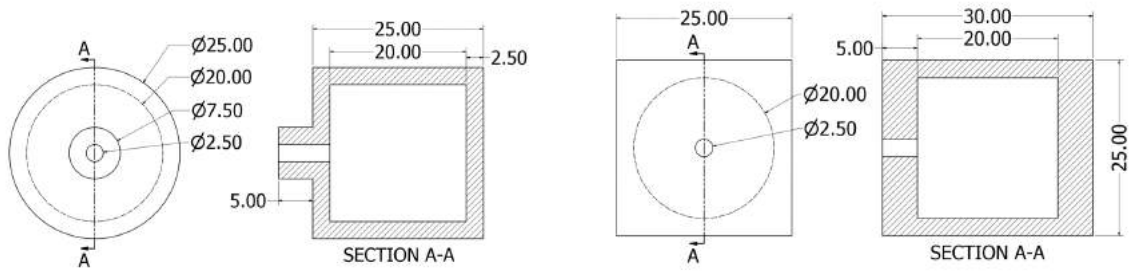

(a) Protruding neck

(b) Cuboid shape

Figure 16: Resonator design alterations.

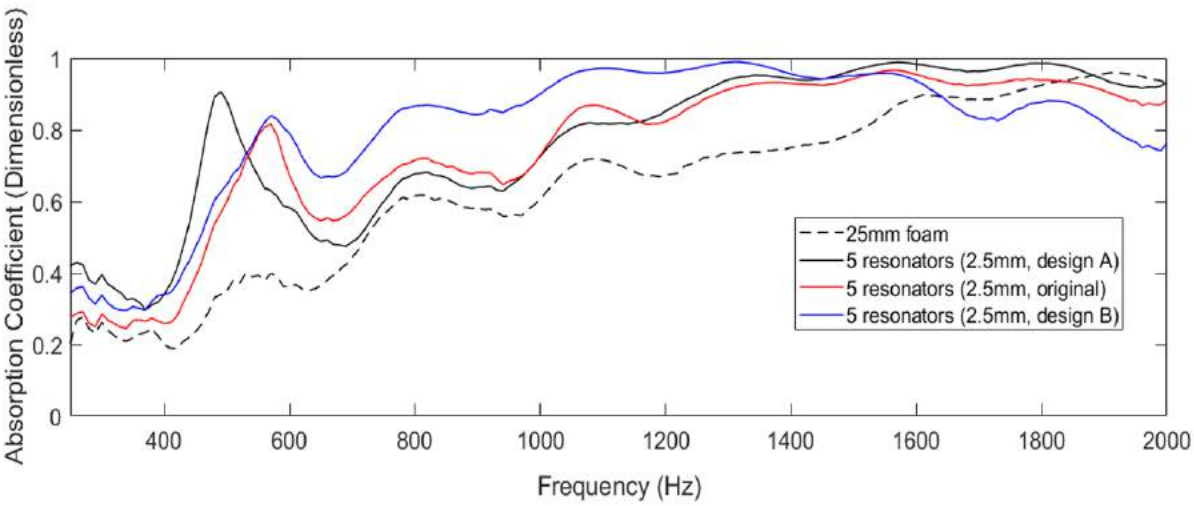

(a) Absorption Coefficient

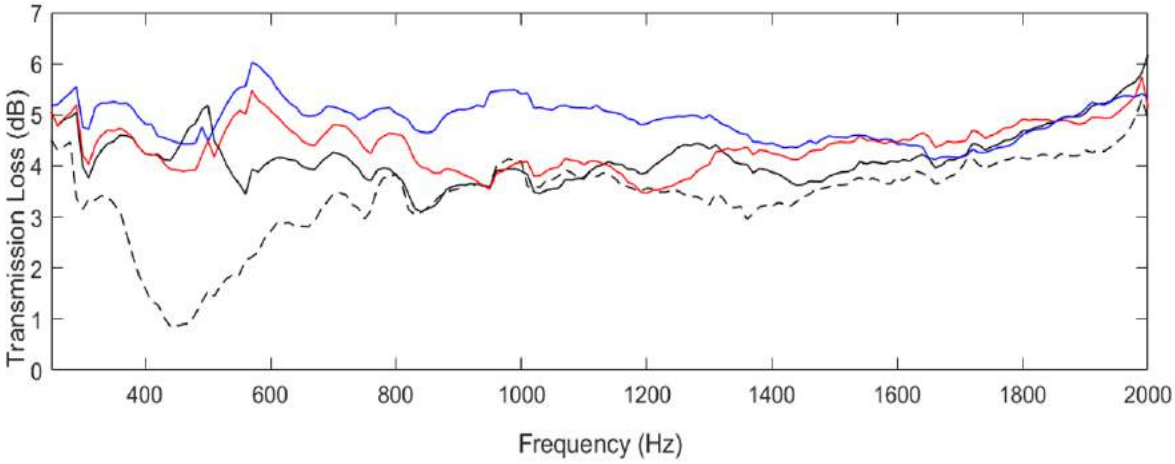

(b) Transmission Loss

Figure 17: Effect of changing the shape of the resonators.

For Design A, due to the increase in neck length, the theoretical resonant frequency should be 500 Hz. This is agreed upon experimentally, with a clear peak seen at 490 Hz. More interestingly, the peak absorption coefficient has increased by 0.1 compared to the original design, but then performs worse after this. The absorption coefficient for the cuboid design (which has the same resonant frequency as the original design), is found to be similar to that of the original. However, there is definite improvement between 600 Hz and 1300 Hz, suggesting a cuboid shaped Helmholtz resonator has better potential for exhibiting high sound attenuation across a broad frequency range.

With regards to STL, the Design B metamaterial outperforms the original design substantially between 800-1300 Hz. On the other hand, Design A performs worse. It is thought this is due to the difference in resonator volume size between the designs. This finding is in agreement with Slagle [9], who found that resonator volume size has the biggest effect on STL.

3.2.5 Mass of Resonators

In many applications where sound reduction is desired, it is vitally important that lightweight solutions are found – for example in aeroplanes. Therefore, it was decided to investigate whether the mass of the resonators has an effect on sound absorption. The mass of the resonators was changed by varying the density of the 3D prints. Two sets of 5 geometrically identical Helmholtz resonators were printed with 10% and 100% infill and embedded into the foam. The infill change results in a mass difference of 5 g per resonator, giving a total mass difference of 25 g. The results of absorption coefficient and STL are given in Figure 18.

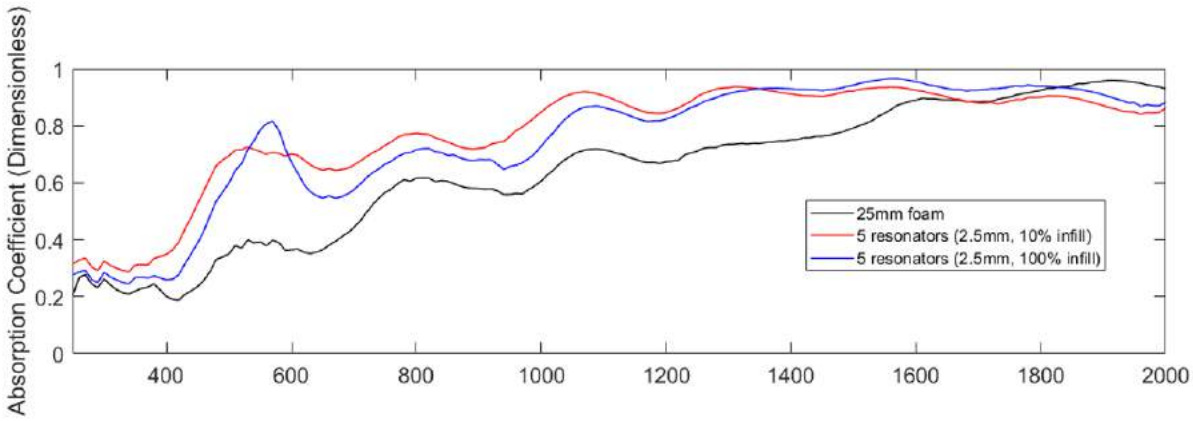

(a) Absorption Coefficient

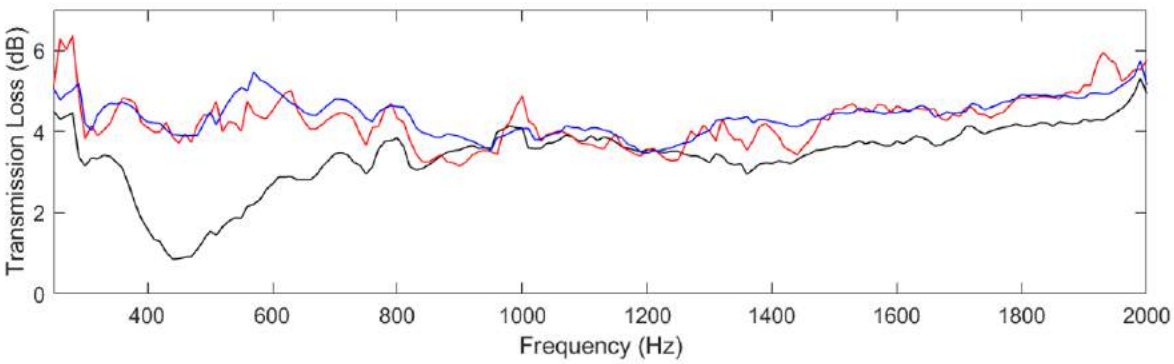

(b) Transmission Loss

Figure 18: Effect of changing the mass of the resonators.

Interesting, a peak in absorption coefficient can only be seen at the resonant frequency of 585 Hz for the 100% infill resonator metamaterial. The peak for the 10% resonator metamaterial is shifted to the left by 50 Hz. This is in contradiction to Slagle et al.'s numerical model, which proposed that a decrease in density would shift the absorption peak to higher frequencies [9]. This contradiction could be due to the fact that the extremely low infill used for the 10% resonators resulted in the 3D print being of a lower quality causing it no no longer acting as a perfect Helmholtz resonator. Despite this, the 10% resonator sample out performs the 100% sample between 600 and 1310 Hz. These results are promising, as they suggest that sound absorption of the HG metamaterial can actually be slightly increased by reducing the weight of the sample.

3.3 Explanation of Hybrid Metamaterial Design

As explained in Section 1.2.2, hybrid acoustic metamaterials can be manufactured using a combination of several structural techniques. The major aim of studying hybrid metamaterials in this study is to construct and test a perforated honeycomb-corrugation hybrid metamaterial (PHCH), inspired by Tang et al. [7] (see Figure 3). Tang et al.'s metamaterial was redesigned to allow it to be fabricated using a 3D printer and able to be tested in the circular impedance tube: this involved printing the metamaterial in two halves due to printer limitations, and using a circular rather than square cross-section. The PHCH metamaterial that Tang et al. found the best performance with has dimensions: a 2 mm top facesheet thickness, 0.4 mm hole size and 60 mm H-C core height. Due to the printing limitation, the parameters we used in the metamaterial were: 2 mm top facesheet thickness, 20 mm H-C core height and both 0.4 mm and 1 mm hole size.

Two different hybrid metamaterials were designed (a 2D and a 3D model) and compared against a baseline model. The baseline's tubes have identical cavity size throughout (Figure 19a). Figure 19b shows the PHCH metamaterial that has been simplified from Tang et al.'s design, as the complicated structure exceeds the resolution possible on the 3D printer. Thus, the number of tubes has been reduced. The 3D hybrid metamaterial is designed to have a cone shaped insert in the honeycomb structure as shown in Figure 19 (c). This insert gives a range of cavity volumes within the tubes and therefore a broader band of absorption. The MPPs are positioned to face the sound source for all hybrid metamaterial samples.

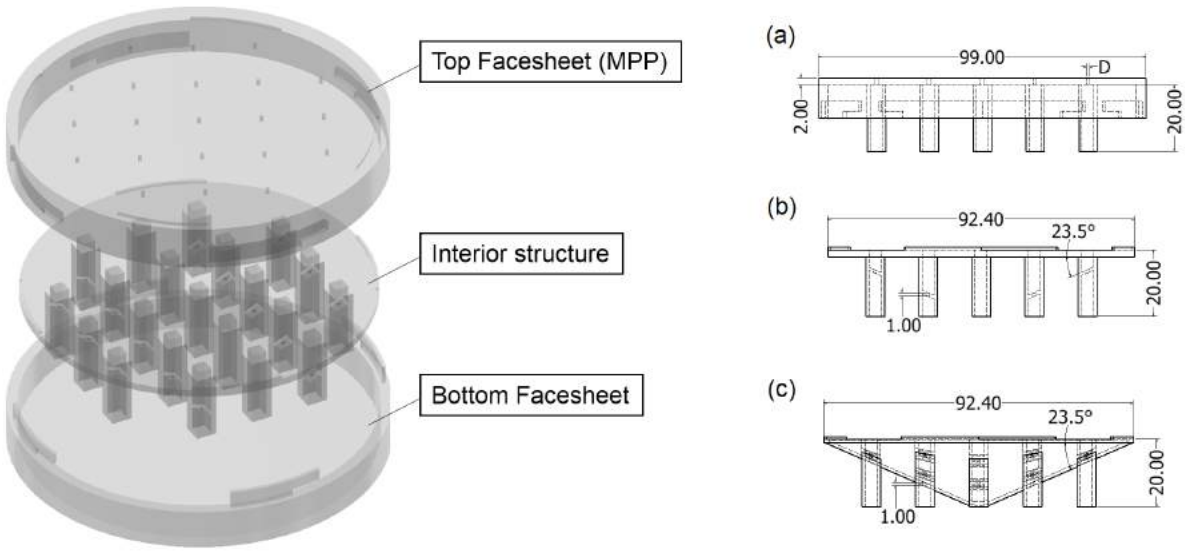

Figure 19: Schematic of hybrid designs (left) and detail of their interior structures: (a) baseline (top facesheet included), (b) 2D, (c) 3D.

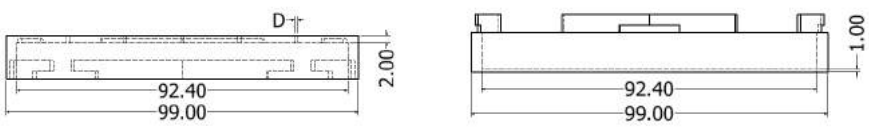

(a) Top facesheet. (b) Bottom facesheet.

Figure 20: Side view of facesheets (a) top (for 2D and 3D only), and (b) bottom (for all designs).

3.4 Experimental Results & Discussion

Figure 21 shows the absorption coefficient for the 2D and 3D hybrid metamaterials with 0.4 mm micro-perforated panels (MPP), compared to the baseline. It is found that both metamaterials have relatively low absorption coefficients, peaking at just below 0.6 for the 3D model and 0.4 for the 2D model. The 2D model only performs better than baseline between 200 and 590 Hz, the 3D model is better from 200-800 Hz and to a much larger degree.

The lower than expected absorption is due to the simplification of the original design: the limit of the 3D printer meant that far less cells had to be used than in the design proposed by Tang et al. [7]. However, this experiment confirms that the introduction of the cone shape insert certainly provides a large improvement in sound absorption between 555 and 990 Hz. Above 1000 Hz, all three designs have similar behaviours – the absorption coefficient decreases as frequency increases.

A numerical study of the 2D design performed in COMSOL predicts this downward trend (Figure 21). However, it is not capable of predicting the peaks since the Thermo-acoustics model (explained in Section was only applied in the resonator chambers. Pressure acoustics will always give a uniform plane wave in the impedance tube which results in a purely exponential decay. Thus, the numerical results are only used as a general guide to support the validity of the experimental methods used.

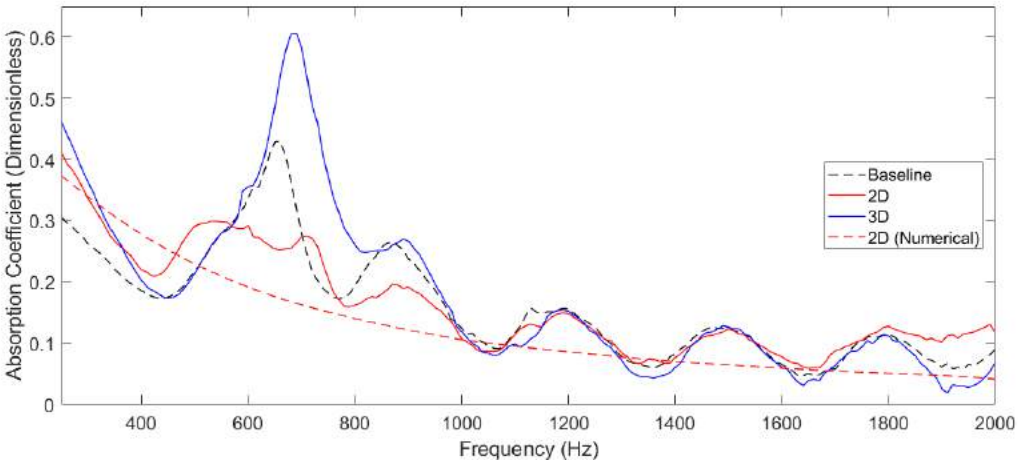

Figure 21: Absorption coefficient of hybrid metamaterial with 0.4 mm MPP.

Three further metamaterials were printed using 1 mm hole size in the MPP to see how this affected the absorption. This change reduced the peak absorption for the 3D and 2D models to 0.51 and 0.33 respectively (Figure 22). However, both peaks are now broader, especially the 3D design. The 3D design now significantly outperforms the baseline case over a wide range.

Interestingly, all three cases now have another peak located at around which is much less prominent in the 2D and 3D cases. The increased size of perforated holes has created this resonant frequency. However, in the 2D and 3D designs a reduction in number of any given cavity size causes the broadening and lowering of peaks. This behavior agrees what has been discussed before in the heterogeneous metamaterials section — the number of resonators at a particular size affects the sound absorption effect at there resonant frequency (Figure 22).

Moreover, another numerical study of the 2D design with a 1 mm MPP is performed. Again, the numerical results reproduce the overall experimental trend found.

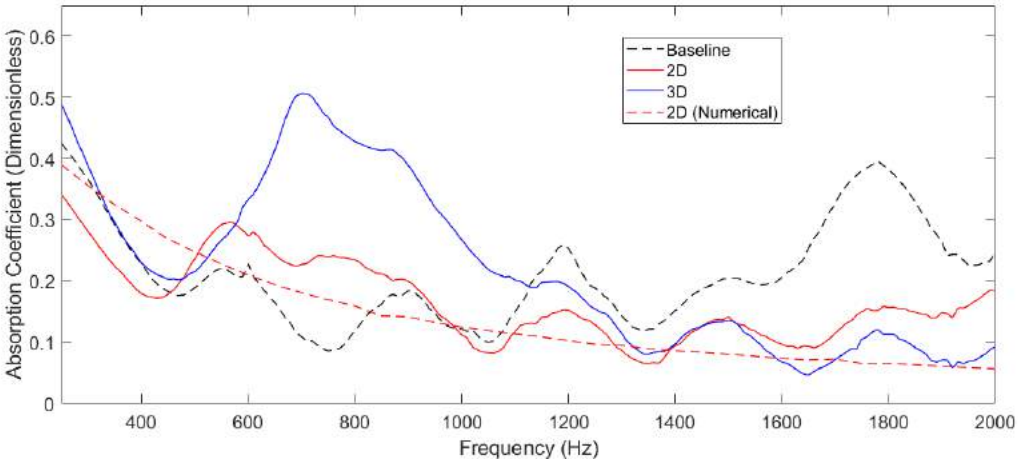

Figure 22: Absorption coefficient of hybrid metamaterial with 1 mm MPP.

4 The Study of Labyrinth Metamaterials

For sound to transmit through a labyrinth metamaterial it must traverse a significantly longer path than through a regular material. This effect is called space-coiling and is what gives labyrinth structures their meta-behaviour. This section will present results from 1D impedance tube and 2D waveguide tests to analyse STL and refraction angle respectively. The 1D tests have been conducted with four different unit cell designs and the 2D tests with micro- and macro-scale structural changes.

4.1 Explanation of Labyrinth Design

4.1.1 Individual Unit Cell Design

A metamaterial that uses space-coiling to creative negative index was first proposed by Liang et al. [5]. Using space-folding metamaterials, rather than locally resonating metamaterials, presents two main advantages. The first is that negative index can be produced across a broad frequency range (over 1000 Hz) as apposed to metamaterial designs such as the ones suggested in Section 2, which only produce negative index across a narrow frequency band near the resonating peak [21]. Furthermore, locally resonating metamaterials are generally designed to exhibit high absorption loss, whereas space-coiling designs can be tailored to reduce loss when necessary.

Such space-coiling designs work by forcing the acoustic wave to travel in subwavelength folded channels which greatly increases the path length of the wave. As acoustic waves are scalar fields, the wave is still able to propagate freely in the curled space [5]. Macroscopically, this delays the propagating phase. Xie et al. [21] adjusted the dimensions of the labyrinth unit cell proposed by Lie et al. [5] to produce a negative to zero index in the frequency range of 2000-3000 Hz. Figure 23a shows the design of the labyrinth structure, which was replicated on CAD software (Figure 23b) and fabricated using a 3D printer. The blue lines represent walls of the unit cell, and the white is the background fluid (air). Sound waves propagate through the unit cell following a zig-zag path, such as the one shown in red from A to C in Figure 23a. This results in a path length approximately 4 times greater than a sound wave that would travel in a straight line from A to C. A longer path length results in a larger phase delay, a property essential for producing negative refractive index.

The 1D impedance tube described in Section 2.2 was used to measure STL across the unit cell. Three further unit cells were designed and fabricated to see how their performance compared with the original design. These designs can be seen in Figure 24. The results of these experiments are detailed in Section 4.2.1.

4.1.2 Prism Design

The second experiment performed by Xie et al. demonstrated that the labyrinth unit cells can be assembled together in a structure to generate a metamaterial than could be usable in real devices [21]. This was proved by taking two-dimensional prism-based measurements to demonstrate negative refraction.

The metamaterial proposed by Xie et al. consisted of a specific arrangement of 55 identical labyrinth unit cells (Figure 25a). Adjacent unit cells were turned upside down in order to lessen the gap between the cells and produce a more symmetrical structure. Xie et al. confirmed that doing so would not edit the dispersion characterises of the metamaterial [21]. The top surface

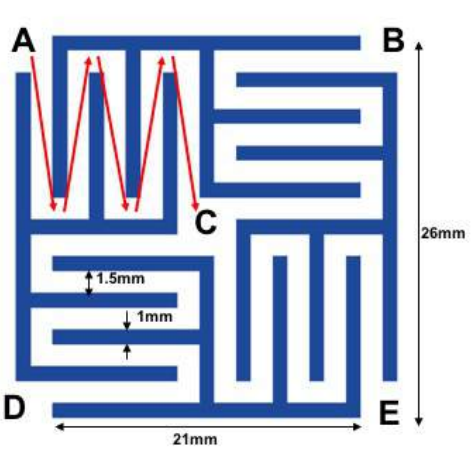

(a) Schematic design of original labyrinth unit cell. Red arrows indicate the path the sound wave would follow.

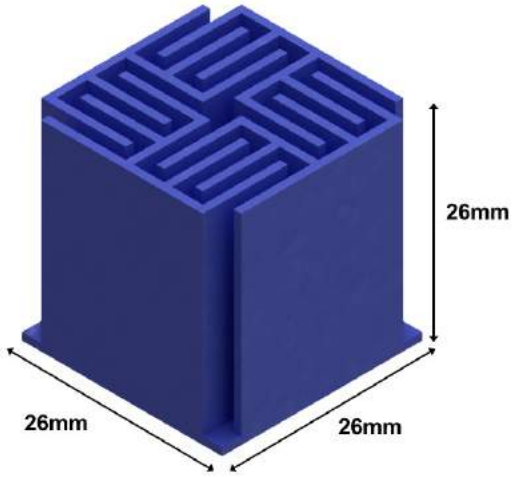

(b) CAD model of unit cell.

Figure 23: Labyrinth metamaterial unit cell design.

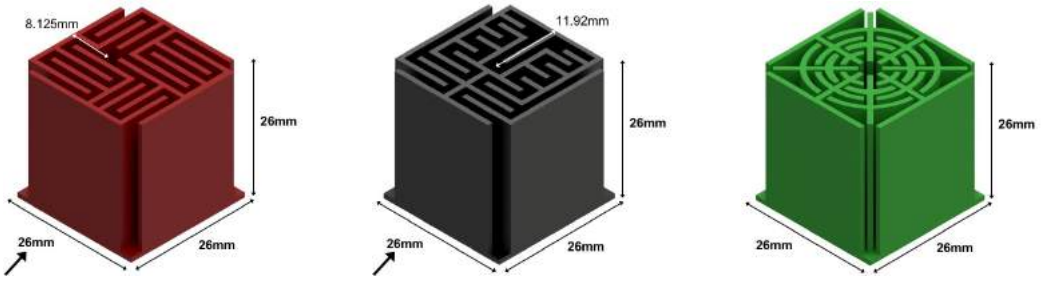

(a) Redesign 1 (b) Redesign 2 (c) Redesign 3

Figure 24: Labyrinth metamaterial redesigns (arrow indicates direction of highest STL for non-symmetrical redesigns).

of the prism was then sealed with a lid to minimise wave pressure leakage. This prism was replicated on CAD and fabricated using a 3D printer.

This experiment was carried out using our 2D waveguide using the method described in Section 2.3. Design choices for Figures 25b and 25c, which were also tested in the 2D waveguide, are also explained in Section 2.3.

4.2 Experimental Results & Discussion

The key objective of this paper for the labyrinth metamaterial design is to replicate the results produced by Xie et al. [21]. The transmission loss across the unit cell is investigated using the one-dimensional impedance tube described in Section 2.2. Then, the two-dimensional waveguide described in Section 2.3 is used to demonstrate that a prism composed of 55 labyrinth unit cells can demonstrate negative refraction. Changes to unit cell design and prism structure are also tested to help develop an understanding of how simple design changes can be used to engineer specific acoustic properties.

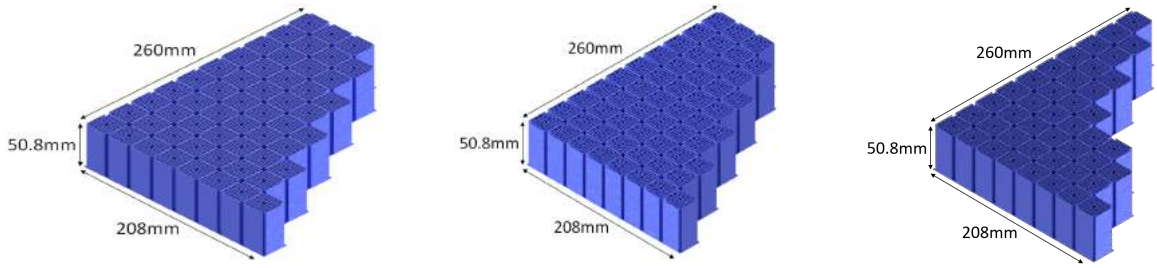

(a) Prism with 55 original unit cells

(b) Prism with 55 redesign 2 unit cells

(c) Restructured prism with 43 original unit cells

Figure 25: CAD Models of assembled prisms.

4.2.1 One-Dimensional Impedance Tube

Figure 26a shows the experimental results from the 1D impedance tube for normal incidence transmission loss (STL) between 1000-3000 Hz. All unit cells are tested in the orientation found to have the highest transmission loss as indicated in Figure 24. The empty tube - represented by the pink dotted line - has a very low transmission loss (<2 dB) suggesting that there is minimal leakage from the impedance tube. The blue dotted line represents a homogeneous block of identical volume to the metamaterial unit cells. This shows a steady transmission loss (5-10 dB) across all frequencies.

Redesign 3 is found to have a significantly lower STL than the homogeneous cube across the whole frequency range. It is thought that this could be due to the lack of 90 degree turns that, if present, would force the sound to reverberate inside the sample more, allowing chance for destructive interference. Due to its lack of high transmission loss this design has not been investigated further.

It can be seen that the original metamaterial design (blue line) has a significantly higher STL than the homogeneous block across a broad frequency range (1800-2500 Hz), despite a reduced density (51% less), suggesting the metamaterial is performing as desired. A peak in transmission loss can clearly be seen at 2100 Hz which is in perfect agreement with the findings by Xie et al., as well as with the numerical results of Figure 26, further validating the reliability of the impedance tube. The performance of the original metamaterial design reduces at frequencies above 2500 Hz, with its STL becoming lower than that of the homogeneous block's. However, it can be seen that Redesign 1 performs best in this range, with a higher STL than the original design. A clear spike can be seen at 2530 Hz (42 dB). Redesign 2, which has a 52% lower density than the homogeneous block, has a higher STL than the homogeneous block from 1600-2100 Hz. It outperforms the original metamaterial design between 1500-1850 Hz, with a peak of 28 dB at 1740 Hz.

Interestingly, all three metamaterial designs converge to a similar transmission loss below 1300 Hz, despite this still being well above the impedance tube's lower frequency limit. All three metamaterials maintain approximately constant transmission loss (5-10 dB) until 400 Hz is reached (not shown on the graph) where the data becomes noisy, likely due to the poor performance of the speaker in this low range as it has a 150 Hz minimum producible frequency. It is believed that this convergence may be due to the channels in the labyrinth now being too small for the sound (260 mm wavelength versus 1.5x10 mm channels) to propagate through effectively. The sound then 'sees' the sample as a roughly homogeneous block. The low range experimental results are supported by evidence in Section 4.2.2 and further discussed later in this section.

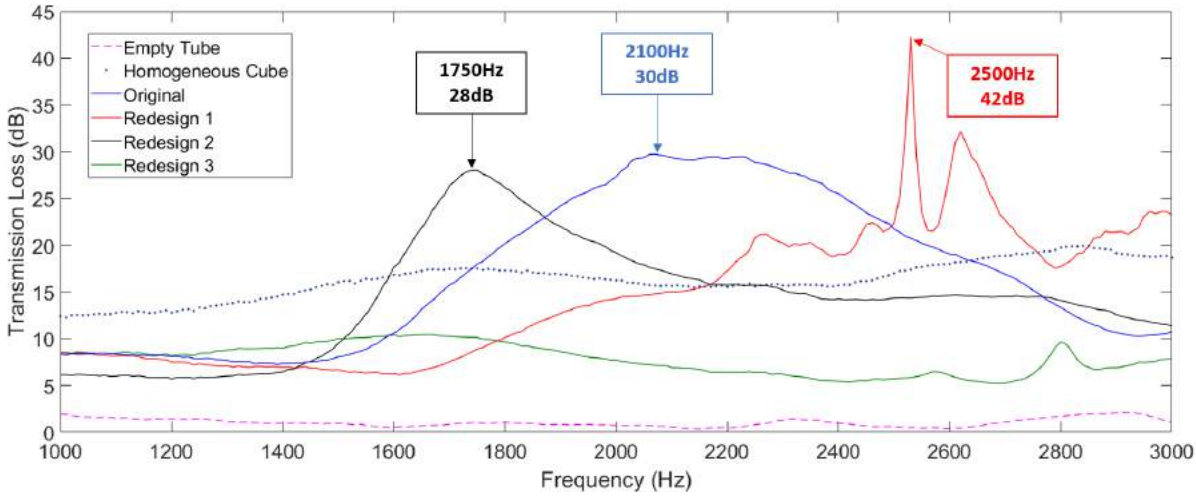

(a) Experimental impedance tube results

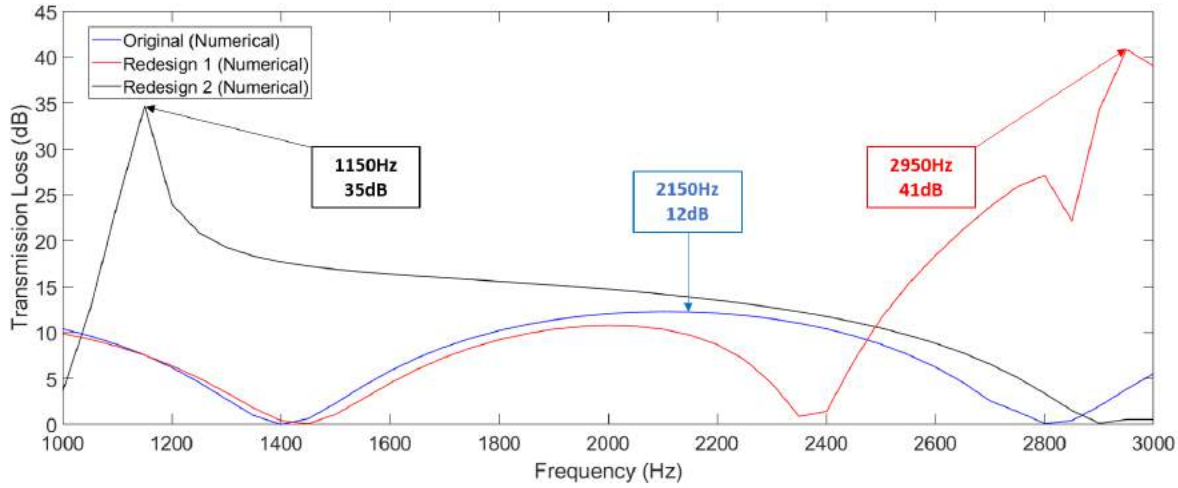

(b) Numerical Results

Figure 26: Transmission loss of single labyrinth unit cells.

The results from Figure 26a can be used to validate our 1D impedance tube by observing low leakage from the empty tube measurements, and replicating the peak in transmission loss at 2100 Hz found by Xie et al. for the original design. It can be concluded that the original design, Redesign 1 and Redesign 2 all exhibit high transmission loss across a broad frequency range. As the study of acoustic metamaterials largely concerns the reduction of low frequency noise, it was decided that no further study would be conducted on Redesign 1 due to its low performance at lower frequencies. Both the original design and Redesign 2 are studied in Section 4.2.2.
The transmission loss of three of the unit cell designs was also obtained numerically and is shown in Figure 26b. Both experimental and numerical methods predict a peak STL at 2.1 kHz but disagree on the magnitude by a factor of almost three. The numerical simulation for Redesign 1 and 2 follow the general shape and magnitude found by the experimental results, however there is a disagreement in terms of matching frequencies.

Despite this, the general trend for transmission loss for all three designs has been captured. Discrepancy between matching exact values in terms of Decibels and Hertz could be due to several reasons. An obvious cause would be leakage in the impedance tube as limitations on how well it could be sealed could affect the experimental results. Another cause could be due

to thermo-viscous losses in the experimental tube which are not accounted for in the numerical simulation.

Overall, the objectives for the impedance tube tests for the labyrinth metamaterials have been achieved. The STL behaviour of labyrinth unit cells can be easily and accurately obtained in the impedance tube. These results are in good agreement with those of Xie et al. for their unit cell design and, alongside this, a unit cell has been designed that outperforms the original design below 1850 Hz.

4.2.2 Two-Dimensional Waveguide

Four experiments were carried out using the 2D waveguide set-up. The aim of the first experiment was to replicate the results produced by Xie et al. which demonstrates that the prism composed of 55 original unit cells exhibits negative refraction. This structure was tested at 2100 Hz as this was the frequency where both parties found the highest STL. The experimental results for this experiment are shown in Figure 27a. It can be clearly seen that the prism bends the transmitted wave towards the same side as the incident wave, indicating negative refraction. The experimental results in Figure 27a impressively replicate the measured field pattern obtained by Xie et al., shown in Figure 27b.

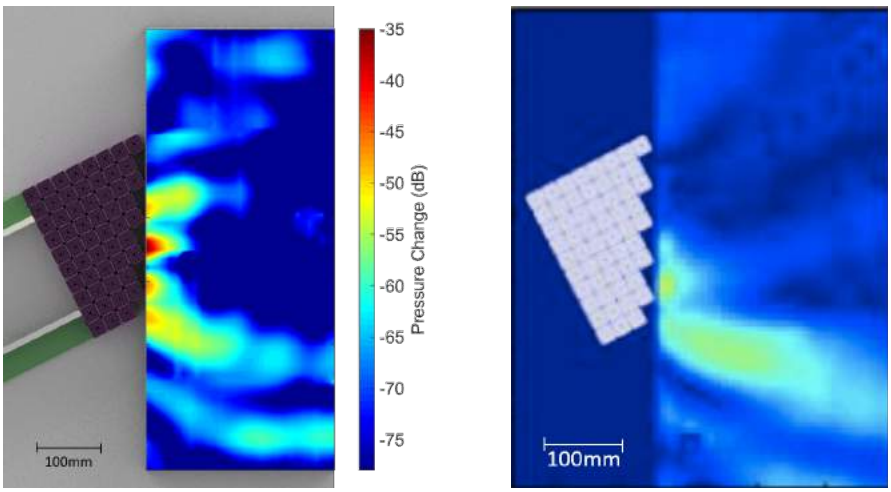

(a) Experimental Results

(b) Results by Xie et al. (Reproduced from [21])

Figure 27: Experiment 1 – Measured field patterns at 2100 Hz with original structure and unit cells (measuring area 0.3x0.7 m).

The second experiment involved editing the structure of the original prism model (see Figure 25c) to achieve a more negative transmission angle at 2100 Hz, as predicted by numerical simulations (Figure 28b). The details of the structure change and the explanation behind it can be found in Section 5.2.2. Figure 28a shows an increased transmission angle compared to the results found by Xie et al. with a significantly larger percentage of the transmitted sound field being negatively refracted.

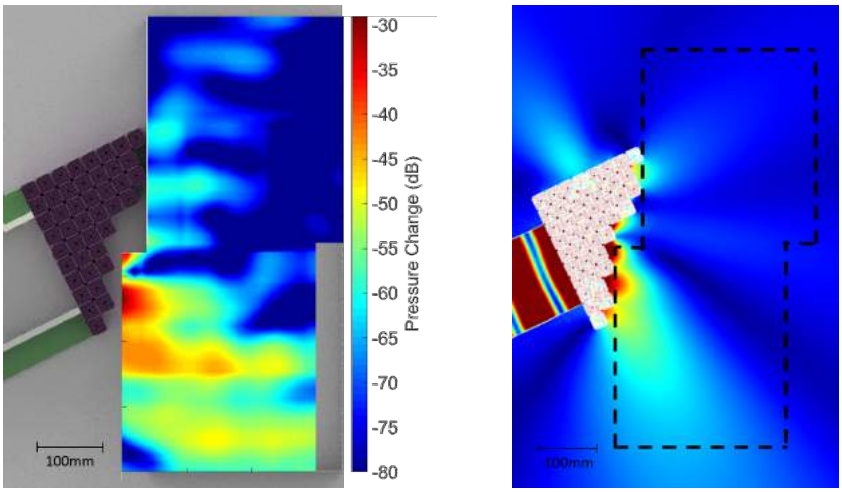

(a) Experimental Results (b) Numerical Results

Figure 28: Experiment 2 – Measured field patterns at 2100 Hz with original unit cell and a changed structure. Note; the measuring area has been shifted to better capture the resulting field.

The third and fourth experiments investigated the original prism layout, but with the unit cell being changed to Redesign 2 (Figure 25b). These experiments were carried out to understand whether changing the unit cell is an effective way of changing the transmission angle. The frequency was initially maintained at 2100 Hz for experiment three for consistency. Numerical simulations suggested that there should be positive refraction (Figure 29b). Figure 29a shows the results of this experiment. As can be seen by the colour bar, very little sound is actually transmitted by the prism (a maximum of -67 dB compared to -30 dB in Figure 27a), making background noise and reflections significant. Therefore, little can be concluded about the angle of transmission.

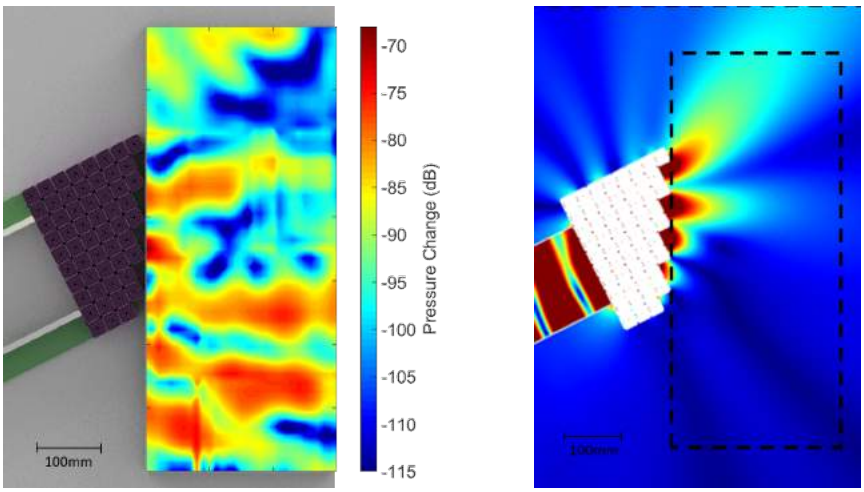

(a) Experimental Results (b) Numerical Results

Figure 29: Experiments 3 – Measured field patterns with original structure and design two unit cells at 2100 Hz.

In order to obtain more useful results, the frequency was changed to 1150 Hz for experiment four. This frequency was chosen as experimental results showed a low STL for this value (6 dB). Figure 30a shows that more sound has been transmitted (as expected) which is in agreement with the experimental results. It also shows that the transmitted sound field has a zero to positive refraction. The isolated area of high pressure at the bottom of Figure 30a is deemed to be due to reflection from the open side of the plate by the traverse. These findings are in disagreement with the high STL predicted by numerical analysis as shown in Figure 30b, as previously discussed in Section 4.2.1.

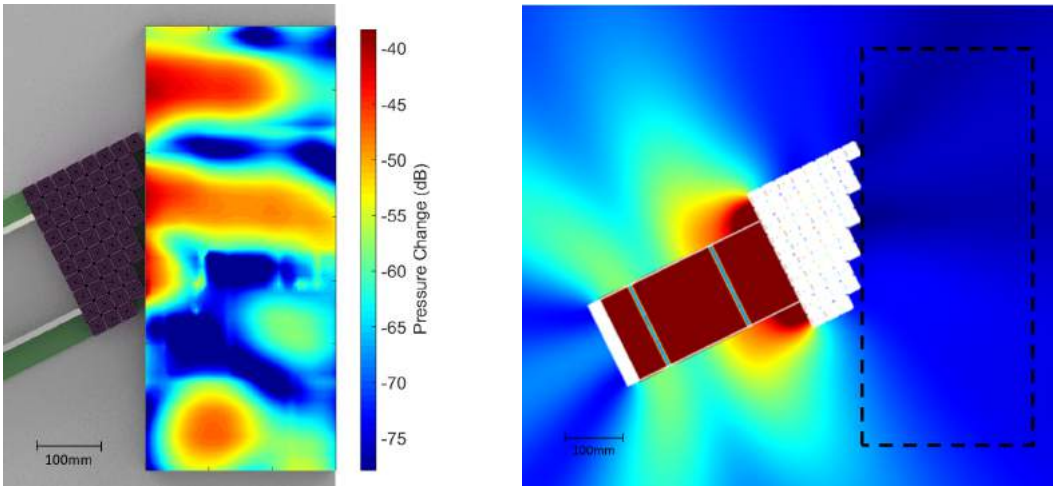

(a) Experimental Results (b) Numerical Results

Figure 30: Experiments 4 – Measured field patterns with original structure and Redesign 2 unit cells at 1150 Hz.

Overall, the four experiments performed in the 2D waveguide show mostly positive results. The sound field produced in the first experiment strongly replicates those produced by Xie et al., validating our waveguide design and method, and proving that the prism produces negative refraction. The second experiment using the improved structure produces an even stronger negative refraction. The experiments performed when the unit cell was changed to Redesign 2 are in agreement with the experimental findings for STL in Section 4.2.1 and highlight the possibility of unit cell change as a route to designing angle of refraction. Section 5 further discusses the causes of this sections results.

5 Numerical results and discussion

This section will describe the numerical models used in this study and discuss the mesh-independent results they produce for both hybrid and labyrinth metamaterials.

5.1 Hybrid Metamaterials

5.1.1 Description of Model

To model hybrid metamaterials, the principles of the Pressure Acoustics (PA) model described in Section 2.4 were applied. A 3D geometry of the cylindrical impedance tube, where its boundaries are once more treated as hard walls is created. However, the PA model can only simulate the STL of a metamaterial due to its geometrical properties, where the energy loss of the transmitted wave occurs due to reflection. In the two microphone set up for the hybrid metamaterial, there is no transmission of the sound waves and the PA model would not be sufficient to account for the absorbed energy. Thus, the implementation of an additional Thermo-acoustics model was proven to be essential in order to simulate the absorptive properties of the geometry [7].

The model solves the system of four equations (continuity (32), momentum (33), energy conservation (34) and the linearised equation of state (35)), which include three additional variables: the velocity u, the temperature, T and the viscosity of the fluid, μ [38].

$$i\omega\rho = -\rho_0(\nabla \cdot u), \tag{32}$$

$$i\omega\rho_0 u = \nabla \cdot \left(-pI + \mu(\nabla u + (\nabla u)^T) + \left(\mu_B - \frac{2}{3}\mu\right)(\nabla \cdot u)I \right) \tag{33}$$

$$i\omega(\rho_0 C_p T - T_0 \alpha_0 p) = -\nabla \cdot (-k\nabla T) + Q \tag{34}$$

$$\rho = \rho_0(\beta_T p - \alpha_0 T) \tag{35}$$

where ρ_0 is the background density, μ_B is the bulk viscosity, C_p is the heat capacity at constant pressure, k is the thermal conductivity, Q is a possible heat source and β_T is the isothermal compressibility.

The Thermo-acoustics model is solved in parallel with the Pressure acoustics model within the domains that it is deployed.

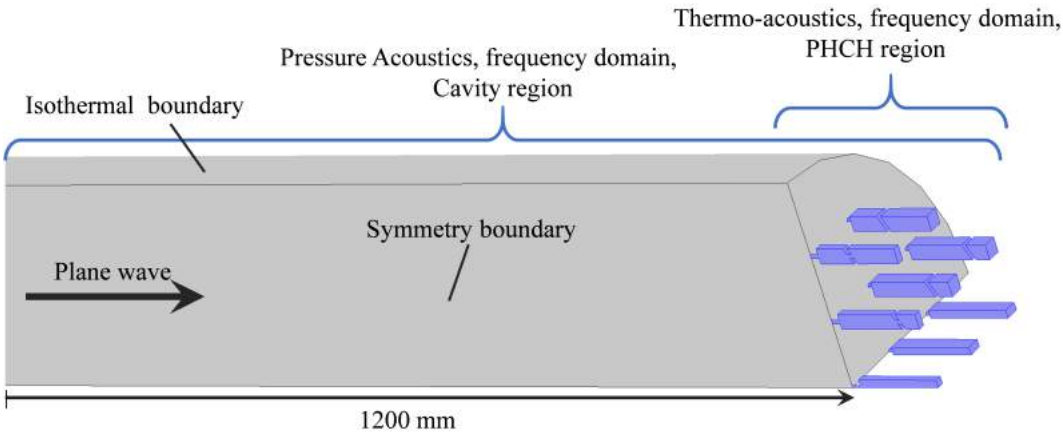

Figure 31: Hybrid metamaterial geometry with the applied physics model sections.

To minimise the computational cost, the Thermo-acoustics model was only applied on the volumes of interest, which in this case are the muffler chambers of the 2D hybrid design as shown in Figure 31 (blue domains). Symmetry boundary conditions were also implemented in order to further minimise the meshed area of the cylinder to one quarter, as shown in Figure 31. Various meshes of increasing density are tested in order to select the one that can produce almost independent results, with minor numerical diffusion error. As shown in Figure 32, a mesh with 200,000 free tetrahedral domain elements can constitute a good compromise between computer cost and accuracy of the results. This mesh is used to simulate the experimental case described below, in Section 3.4.

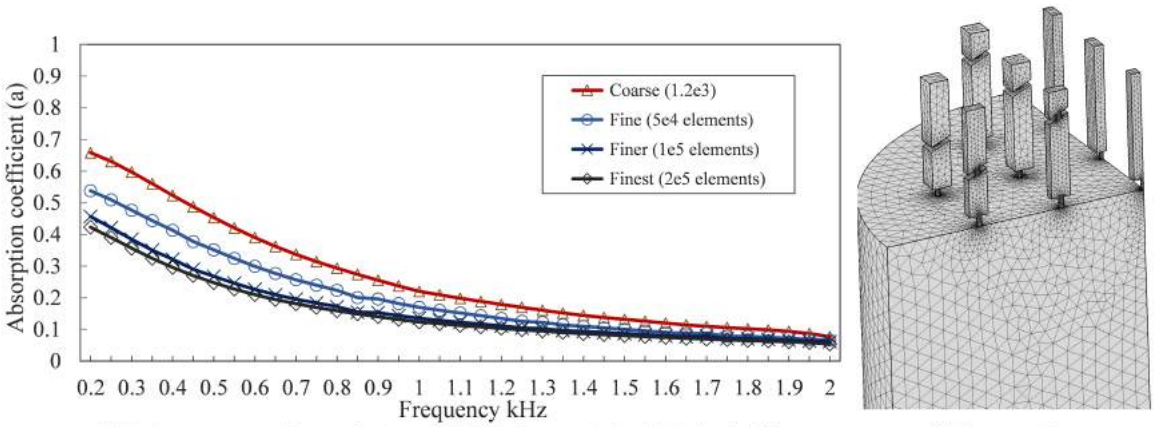

(a) Mesh convergence history for 1mm hybrid design over 0.2 – 2 kHz bandwidth

(b) Finest mesh

Figure 32: Mesh convergence study for independent results.

5.1.2 Results

To investigate the nature of absorption of the metamaterial the comparisons of thermal and viscous energy dissipation are plotted in Figure 33. It appears that viscous dissipation dominates, mainly in the first narrow regions of the non-central mufflers (Fig 33a), where there is a higher power amplitude compared to the central region, as shown in Figure 33c which agrees with the results of Tang et al. The thermal losses of Figure 33b can be considered negligible for this geometry, since they are several orders of magnitude less than the viscous. Generally, the redesigned hybrid geometry shows similar energy loss regions with the original design of Tang

et al., where most of the dissipated kinetic energy lies within the first thin region and this is attributed to the effect of viscous forces. However, our results appear to have a drop of about 2 orders of magnitude, which can be attributed to the thinner duct dimensions that do not allow enough pressure change to propagate up to the second constriction, as shown in Figure 33c. Another dimensional characteristic that can cause large pressure drop inside the ducts could be the relatively small ratio of the total hole area to the impedance tube cross-sectional area, which results in the reflection of most of the energy while allowing only a small percentage to go through the muffler inlet holes.

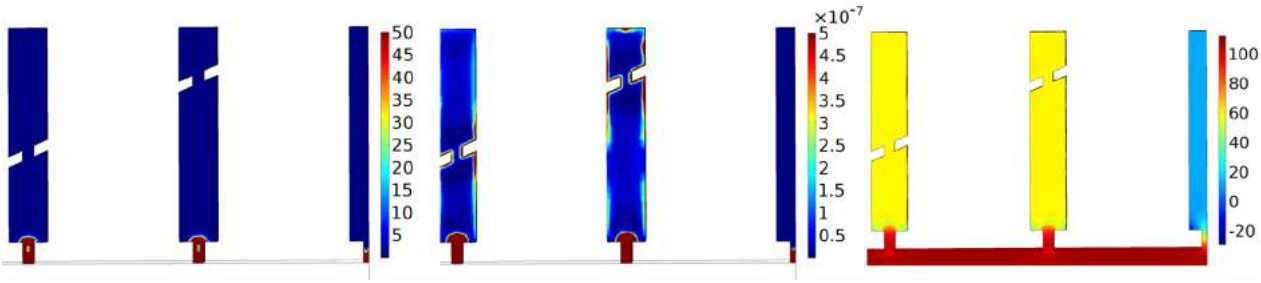

(a) Viscous losses (W/m^3)

(b) Thermal losses (W/m^3)

(c) SPL variation in the impedance tube (bottom) and ducts in dB at 200 Hz

Figure 33: Thermo-acoustic model results of hybrid metamaterial muffler chambers.

5.2 Labyrinth Metamaterials

5.2.1 Description of Model

The numerical simulations for the 1D and 2D labyrinth designs were performed in the frequency domain for parametric sweeps of 0.5-3 kHz. A mesh-dependence study is also conducted for the 1D design in order to select the appropriate mesh for the simulations. The results in Figure 34c show the variation of pressure in some selected points of the 1D computational domain (Figure 34a), as function of the mesh resolution. Based on these results, a mesh with average cell size of less than one mm (1.2 elements/mm^2) is finally selected.

Figures 34a and b show the meshed areas for the 1D and 2D cases respectively. For the 1D plane wave cases, all the surfaces were treated as hard wall boundaries, except of the rectangular duct inlet, where Plane Wave Radiation condition was applied and the outlet, where Perfectly Matched Layer (PML) condition was implemented in order to prevent any reflection into the duct, thus simulating the far field region. Similarly, in the 2D simulations the plane wave radiation condition was applied on the waveguide inlet and the Perfectly Matched Layer boundary condition was applied on all four side regions of the simulated area.

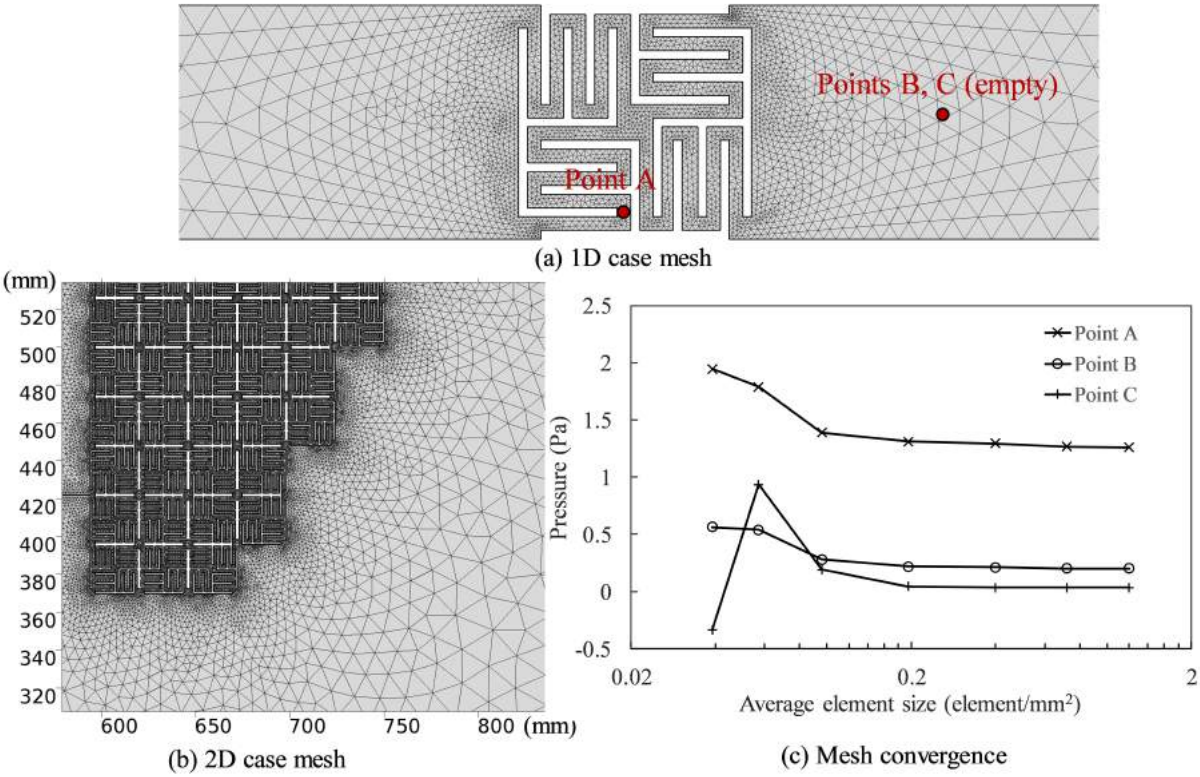

Figure 34: Schematics of 1D and 2D meshes and convergence for the 1D case.

5.2.2 Results

To verify the results obtained in [21], the original 2D geometry was firstly simulated and compared to the numerical results of that paper. As shown in Figure 35 our computational results are in good agreement with Xie et al.'s results, as well as with our experimental data shown in Figure 28b. Any deviation from the desired pressure amplitude could be attributed to the idealised boundary conditions (e.g. hard wall boundary almost attenuates sound waves completely at the top and bottom outer regions of the waveguide), which do not account for any thermo-viscous losses. However, the transmission angle seems to agree, both showing a negative refractive index.

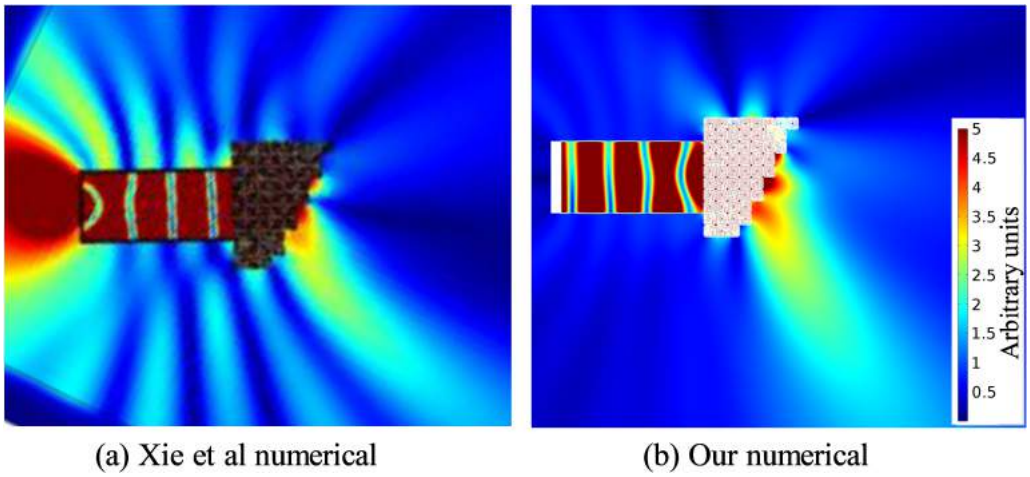

Figure 35: Numerical results (Reproduced from [21]) (a) compared with ours (b).

Initially, an array composed of 10x10 original unit cells was simulated for multiple frequencies. These simulations verified that the transmission angle depends largely on the appropriate placement of such units in each row, and not on their particular geometry, as shown in Figure 36a. Consequently, to verify that, the original configuration was simulated but with no interaction between rows (by adding row isolation layers), as shown in Figure 36b. Although the resulting pressure profile is not identical to the original, the transmission angle appears to remain about the same. The wave is restricted to only travel through the channels along the x-axis, and this results in lower energy attenuation from the top and bottom sides, creating a more inflated pressure profile after the line of incidence.

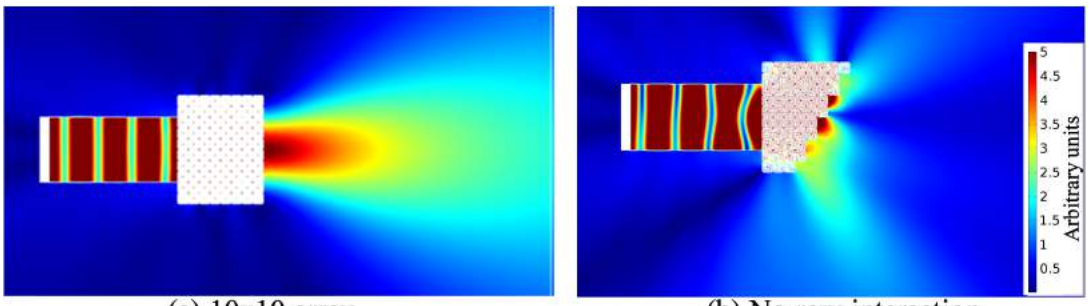

(a) 10x10 array (b) No row interaction

Figure 36: Further numerical results for rectangular 10x10 arrays design (a), and with no interaction between rows (b).

The above simulated cases indicate that the transmission angle mainly depends on the total path length of the labyrinth rows that extend on the same direction as the acoustic wave of the plane source. Thus, to further understand the properties of such geometries, their effect on the pressure phase had to be analysed. Figure 37 shows the phase change for a 1D row of 1 to 8 labyrinth units for the Original and the Redesign 2 at 2100 Hz. Experimental work was also implemented to support the findings for up to 3 consecutive units of both geometries, and the agreement is very good in almost all cases, as shown in Figure 37.

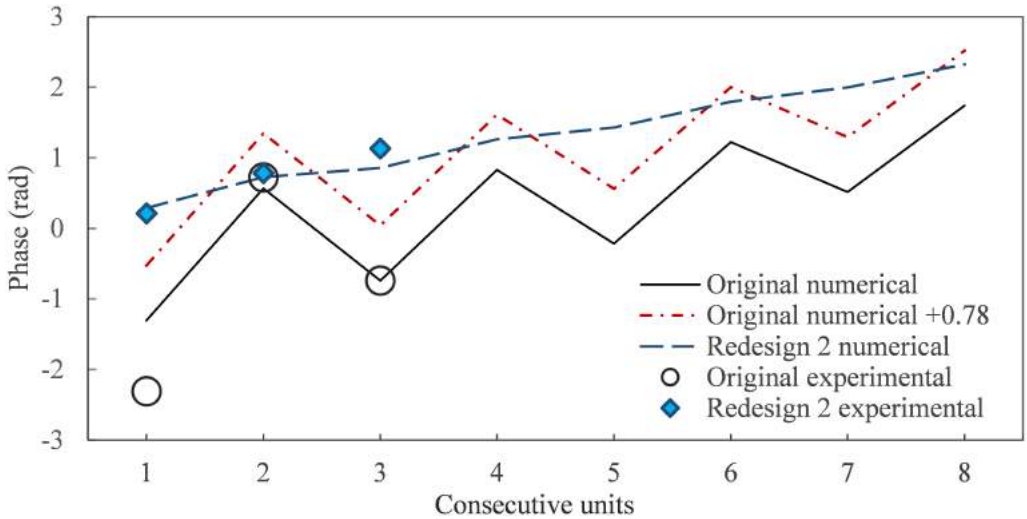

Figure 37: Phase variation as the number of units in a 1D row increases.

It appears that for both designs, the phase increases linearly as the number of odd or even units increases. However, the derivative between two successive nodes changes sign, especially

in the case of the original design, which at the frequency of 2.1 kHz has its STL peak, as shown in Figure 37. However, the phase difference of two successive nodes of the original design appears to maintain a constant value at π rad, which could lead to wave cancellation through the destructive interference of the propagating waves from each exit that lies on the boundary line of the metamaterial.

Wave cancellations do not cancel the energy of the outgoing waves [41] but instead redistribute it within the area that surrounds the labyrinth array. Figure 38b shows the pressure mode of 2100 Hz at which the acoustic waves appear to propagate in all directions but with a higher energy density towards the negative angle of transmission.

Based on the extracted information from Figure 37, one may assume that in order to recreate the same transmission angle of Figure 35 with Redesign 2 type units, the configuration would have to change accordingly. Therefore, instead of keeping the same number of units in each row, a more reasonable approach would be to recreate the phase values of the 'Original' curve of Figure 37 with nodes that lie on the 'Redesign 2 curve'. Assuming that there exists some form of wave cancellation, the interest shall be focused on the relative phase differences between two successive rows. Thus, by vertically displacing the 'Original curve' so that it lies within the range of values of the 'Redesign 2' (Figure 37), the phase values of the 'Original Displaced' curve nodes 3-8 correlate to the nodes 1, 6, 2, 7, 5, 8 of the 'Redesign 2' curve, respectively.

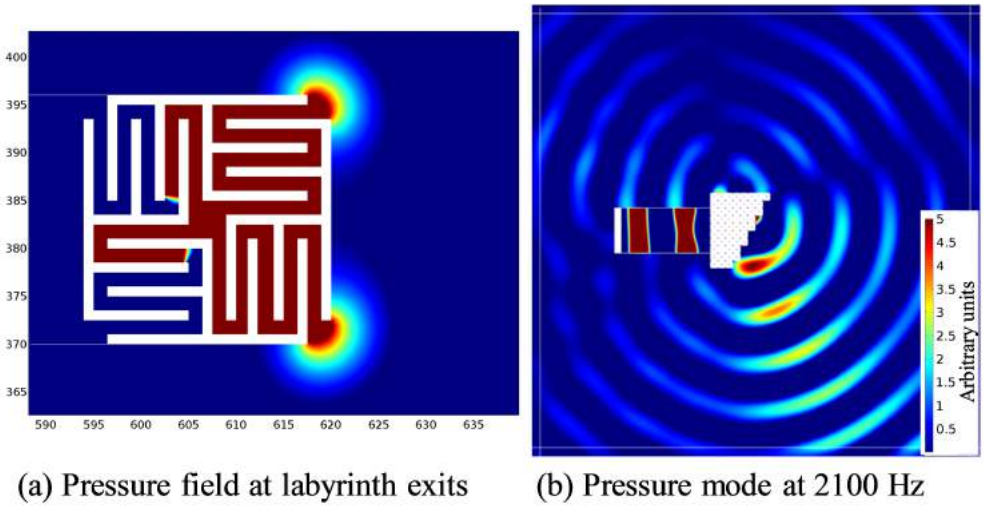

Figure 38: Pressure field (a), and mode (b), at 2100 Hz with original units.

The above configuration is demonstrated in Figure 39a, where the angle of transmission resembles that of the original design, while its negativity is apparent. Unlike the results of Figure 39a, where the adopted configuration is based on the effect that the original labyrinth unit has on the pressure phase, the results of the new configuration in Figure 39b show a more focused acoustic ray towards the negative region relative to the conceivable boundary line, which separates the metamaterial from the environment.

Note that in 1D labyrinth cases, where a negative refractive index is observed, the transmitted (or reflected) fields are handled as individual strips of propagating waves, where energy is not redistributed. Instead, the observer has the impression that the angle of transmission has changed [42]. However, in the 2D cases the waves that exit from each row the metamaterial geometry interact with each other producing cancellation and amplification regions.

However, the resulting transmission of Figure 39b is not ideal due to the fact that the number

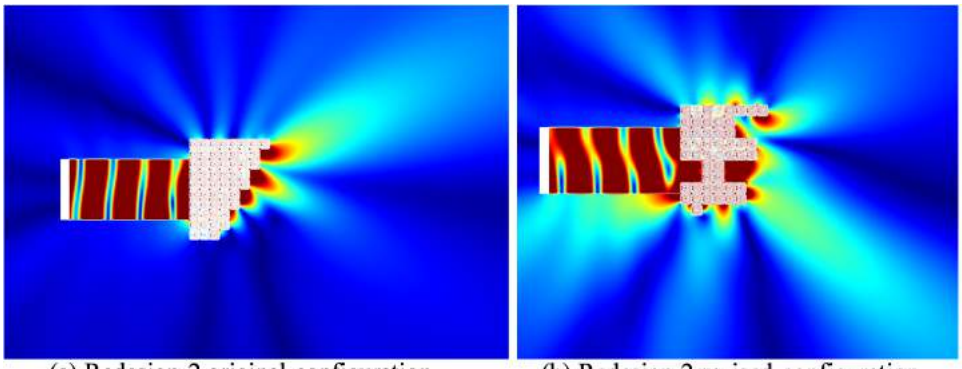

(a) Redesign 2 original configuration (b) Redesign 2 revised configuration

Figure 39: Pressure fields using Redesign 2 units.

of units in each row does not strictly increase from bottom to top. This results in an anomalous boundary between the metamaterial and the environment compared to the original configuration of Figure 35, which affects the exit of the acoustic waves and thus the cancellation regions.

Several simulations of different combinations for the row phase gradient produced an Improved design with even higher index negativity, as shown in Figure 40a. The improved configuration is composed of 43 Original units instead of 55 and has a steeper reduction of units at the middle compared to the linear of the Original configuration of Xie et al. The pressure drop along a vertical line 1 m away from the source (Figure 40a) is plotted in Figure 40b for comparison with the Original design. The numerical findings were also validated experimentally (Figure 28b), which implies that a gradual phase drop of π is desirable but not necessary. However, further analysis needs to be implemented for the understanding of the destructive interferences that take place.

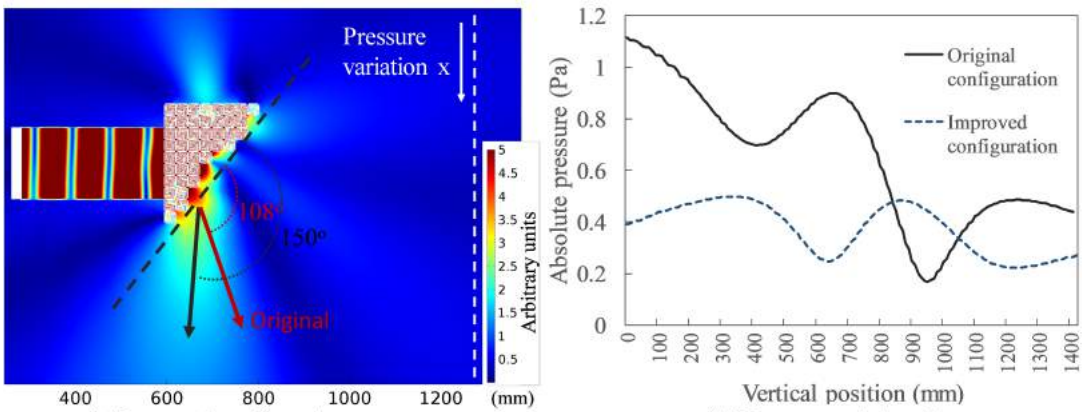

(a) Improved configuration (b) Pressure variation along x

Figure 40: Comparison of transmission angle (a), and of vertical pressure distribution (b), of the original and the improved design.

The above findings indicate that there is a strong correlation between the phase gradient of the labyrinth array rows and the negativity of the transmission angle. Nevertheless, it appears that the waves interference after the labyrinthine exit is a very complex phenomenon, which cannot be easily generalised. This could imply that numerical or analytical methods might always be necessary for the implementation and improvement of such systems.

6 Analytical model

The following analytical model attempts to describe the zig-zag labyrinth geometry sketched in Section 41, which is composed of 5 small regions A, C, E, G, I and 5 bigger regions B, D, F, H, J with dimensions wd and $(l+d)d$, respectively. The dimensions l and d can be calculated from $d = a_x/(m+n) - w$ and $l = a_y - 2t - d$ where m and n are the number of top and bottom labyrinthine teeth, respectively (in this case $m = 3$ and $n = 2$).

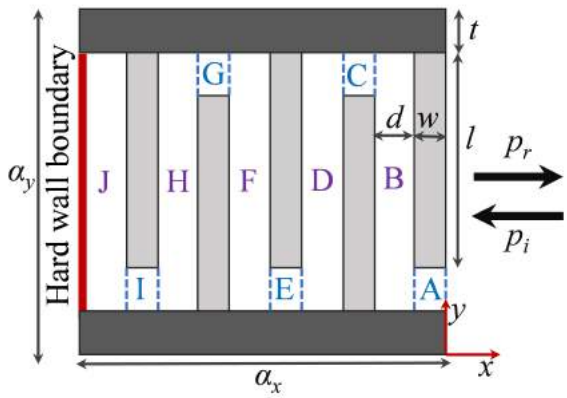

Figure 41: Schematic representation of a closed-end zig-zag labyrinth.

6.1 Derivation

Using the sound wave pressure expression and the relation $ik_0\rho_0 c_0 u = \nabla p$, pressure and velocity of the propagating waves in the channels A, B and C are given as [41]:

$$p_A(x,y) = A^+ e^{ik_0(x+w)} + A^- e^{-ik_0 x}, \tag{36}$$

$$u_A(x,y) = \frac{1}{\rho_0 c_0}\left[A^+ e^{ik_0(x+w)} - A^- e^{-ik_0 x}\right], \tag{37}$$

$$p_B(x,y) = \sum_{n=0}^{\infty} \phi_n(y)\left[B_n^+ e^{ik_{xn}(x+w+d)} + B_n^- e^{-ik_{xn}(x+w)}\right], \tag{38}$$

$$u_B(x,y) = \sum_{n=0}^{\infty} \phi_n(y)\frac{k_{xn}}{k_0\rho_o c_0}\left[B_n^+ e^{ik_{xn}(x+w+d)} - B_n^- e^{-ik_{xn}(x+w)}\right], \tag{39}$$

$$p_C(x,y) = C^+ e^{ik_0(x+2w+d)} + C^- e^{-ik_0(w+w+d)}, \tag{40}$$

$$u_C(x,y) = \frac{1}{\rho_0 c_0}\left[C^+ e^{ik_0(x+2w+d)} - C^- e^{-ik_0(x+w+d)}\right], \tag{41}$$

$$\phi_n(y) = \sqrt{2-\delta_{0n}} cos[k_{yn}(y-t)], \tag{42}$$

where $\phi_n(y)$ is the transverse eigenmode.

The incident field is the sum of the incoming and the reflected wave and is given by:

$$p(x,y) = p_i + p_r = e^{-ik_0 x} + \sum_{n=0}^{\infty} R_n \Psi_n(y) e^{ik'_{xn}x}, \tag{43}$$

The wavenumber along y-direction can be expressed as $k_{yn} = \frac{n\pi}{l+d}$ for $\in N$ and $k_{xn} = \sqrt{k_0^2 - k_{yn}^2}$. The symbols $A^+, A^-, B_n^+, B_n^-, C^+ and C^-$ are the coefficients in the corresponding regions of Figure 41. Note that n denotes the nth mode in all regions identical to B. For higher frequencies the y-dimension of such regions is comparable to the wavelength so normal modes can be employed for more accurate results. However, the frequency below which all modes attenuate completely (cut-off frequency) can be calculated to be roughly 14 kHz (for mode 1) for this or similar Labyrinthine geometries, which was also validated by the numerical simulations: As shown in Figure 42, the resulting wave in the incident region remains almost plane for the frequency of 12 kHz, but not for the higher frequency of 17 kHz.

By applying the continuity of pressure and volume velocity at the interface of regions A/B and B/C (at $x = -w$ and $x = -w-d$, respectively) we can obtain a transfer matrix M_1 that links region A with C:

$$\begin{bmatrix} C^+ \\ C^- \end{bmatrix} = M_1 \begin{bmatrix} A^+ \\ A^- \end{bmatrix}, \tag{44}$$

where,

$$M_1 = \begin{bmatrix} e^{-ik_0 w}(a+c+2D^2)/b & -c/b \\ c/b & e^{ik_0 w}(a-c-2D^2)/b \end{bmatrix} \tag{45}$$

and

$$a = e^{-ik_0 w} 2D \frac{k_0}{k_{x0}} \frac{1+e^{ik_0 d}}{1-e^{ik_0 d}} \Phi_0^2 \tag{46}$$

$$b = 4D \frac{k_0}{k_{x0}} \frac{e^{ik_0 d}}{1-e^{ik_0 d}} \Phi_0^1 \tag{47}$$

$$c = e^{-ik_0 w} \frac{k_0^2}{k_{x0}^2} \Phi_0^2 \tag{48}$$

$$D = \frac{d+l}{d} \tag{49}$$

$$\Phi_n^1 = \frac{1}{d}\int_t^{t+d} \phi_n(y)dy \tag{50}$$

$$\Phi_n^2 = \frac{1}{d}\int_{t+l}^{t+l+d} \phi_n(y)dy \tag{51}$$

Since the connected paths get repeated, it can be shown that:

$$\begin{bmatrix} I^+ \\ I^- \end{bmatrix} = M_1^4 \begin{bmatrix} A^+ \\ A^- \end{bmatrix}, \tag{52}$$

Following the same procedure, the transfer matrix M_2 that connects the incident region with region A is found by the application of both continuity of sound pressure and volume velocity. Thus, it can be shown that:

$$\begin{bmatrix} A^+ \\ A^- \end{bmatrix} = M_2 \begin{bmatrix} 1 \\ R_0 \end{bmatrix}, \tag{53}$$

where,

$$M_2 = \begin{bmatrix} -e^{-ik_0 w}(a'-1) & e^{-ik_0 w}\Psi_0 b' \\ a' & -\Psi_0(b'-1) \end{bmatrix} \tag{54}$$

and

$$a' = \frac{a_y}{2d} + \frac{1}{2}, \tag{55}$$

$$b' = \frac{a_y}{2d}\frac{k'_{x0}}{k_0} + \frac{1}{2}, \tag{56}$$

$$k'_{xn} = \sqrt{k_0^2 - k'^2_{yn}}, \tag{57}$$

$$k'_{yn} = \frac{n\pi}{l+d+2t}, \tag{58}$$

By considering the continuity of pressure and velocity between regions I and J and the hard wall boundary condition at $x = -5d - 5w$ where $u_j = 0$, and combining equations 44, 52 and 53, we get a system of seven equations with seven unknowns ($A^+, A^-, I^+, I^-, J^+, J^- and R_0$), which can be solved with respect to the amplitude R_0 of the reflected wave p_r to give:

$$R_0 = \frac{-e^{ik_0 w}\xi M_{21} + (\xi + 2Dk_{x0}(\Phi_0^1 - e^{ik_0 d}))M_{11}}{e^{ik_0 w}\xi M_{22} - (\xi + 2Dk_{x0}(\Phi_0^1 - e^{ik_0 d}))M_{12}} \tag{59}$$

where

$$\xi = e^{ik_0 d}(1 + Dk_{x0}), \tag{60}$$

$$M = M_1^4 M_2 = \begin{bmatrix} M_{11} & M_{12} \\ M_{21} & M_{22} \end{bmatrix} \tag{61}$$

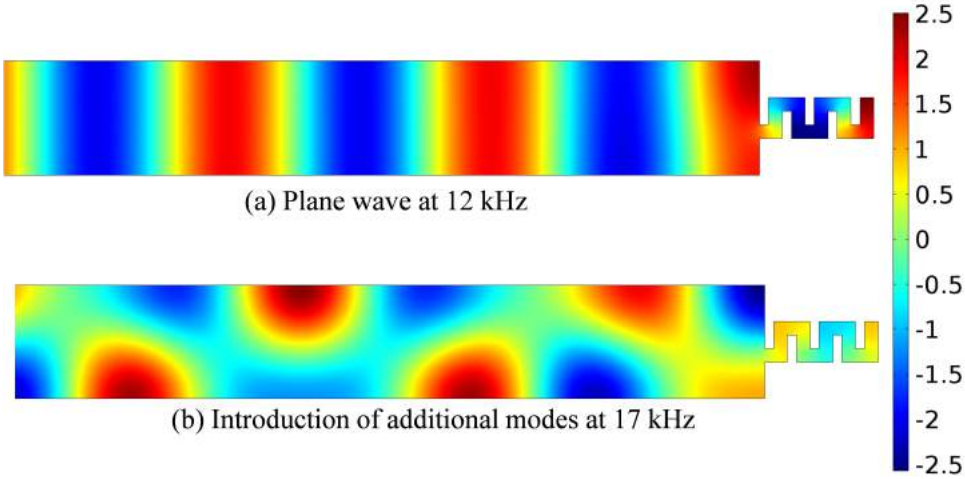

(a) Plane wave at 12 kHz

(b) Introduction of additional modes at 17 kHz

Figure 42: Modal introduction in the duct.

6.2 Model results

The analytical model is tested for its reliability in predicting the phase change due to the total path extension inside the labyrinthine geometry. Figure 43 shows the variation of $arg(R_0)$ compared with the corresponding numerical results obtaind by COMSOL. As shown in this Figure, the analytical model shows a reasonable approximation of the phase change trend, especially for lower frequencies. For higher frequencies the numerical error of the used computational mesh increases, while, on the other hand, the lack of modal analysis in the analytical model affects the accuracy of its results. Consequently, the differences between the two curves increase with the frequency, and hence improvement of the accuracy of both methods results is needed in order to assess the performance and reliability of the analytical model. In this view, the current results are encouraging and show promising possibilities for further application in the optimum design and manufacturing of such units.

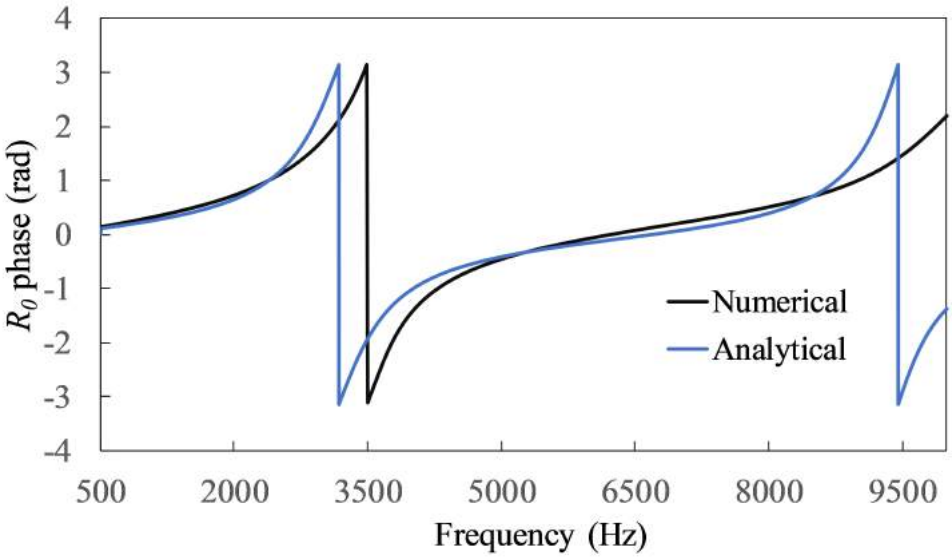

Figure 43: Comparison of Numerical with Analytical results of zig-zag model for $t = 4mm$.

7 Conclusions

Promising results are found for all three types of acoustic metamaterials studied in this report. The combination of experimental and numerical studies has resulted in an improved understanding of the field, successfully meeting the main project objectives.

Both heterogeneous metamaterials and hybrid metamaterials were tested using a circular impedance tube to seek the high sound attenuation at targeted low frequencies and broadband low frequency respectively. A parametric study on the HG metamaterials concluded that increasing the number of resonators embedded in the melamine foam resulted in increased absorption and higher STL. It was found that the HG metamaterial could be easily be designed to exhibit high absorption at desired frequencies by changing the neck diameter of the Helmholtz resonators. Using cuboid resonators was also found to be the most influential way to improve STL across a broad frequency range due to a larger cavity volume size. Finally, it was found that changing the mass of the resonators did not negatively affect absorption or STL of the metamaterial, which is a promising conclusion as most real life applications desire lightweight sound reduction techniques.

Two sets of 2D and 3D hybrid metamaterials were designed with 0.4 mm and 1 mm MPPs. It was concluded that the overall low absorption for all designs was due to the reduced number of cells that had to be used compared to the design proposed by Tang et al. [7]. The restriction was due to limitations of the 3D printer. However, both 2D hybrid metamaterial designs were found to be in close agreement with the numerical simulations for absorption coefficient, and it was clear that the 3D design helped to achieve higher absorption across a larger frequency range.

For studying labyrinth metamaterials, a 1D impedance tube was specially designed and constructed to a high standard to measure the STL across labyrinth unit cells. The labyrinth design, proposed by Xie et al., was found to have a higher STL than a homogeneous block's in the frequency range 1800-2500 Hz, despite having a 51% lower density. Furthermore, a peak in transmission loss was found at 2100 Hz, which is in perfect agreement with the results found by Xie et al. Three further unit cell designs were also tested in the impedance tube, one of which outperformed the original unit cell design in the frequency range 1500-1850 Hz. This experimental study successfully proved that labyrinth designs can be altered and tuned to produce a desired transmission loss across a broad frequency range. Matching trends were found by numerical simulations.

A 2D waveguide was designed and constructed for studying transmission angles of metamaterial prism structures, with the aim of replicating results found by Xie et al. Experimental results successfully reproduced the sound field produced by Xie et al. for the 55 unit cell prism structure at 2100 Hz, showing that the prism impressively demonstrates negative refraction. The similarity between the results prove that the 2D waveguide has been well constructed. Numerical simulations were performed to develop the understanding of phase change across unit cells, and an improved prism design was suggested. Experimental results not only shows that the refraction angle was increased, but also that a greater proportion of the sound field was negatively refracted. Two further experiments involved changing the prisms unit cell design and testing the transmission angle at 2100 Hz and 1150 Hz. Although there is discrepancy with numerical results, the findings confirm that changing the design of the unit cell can change the transmission angle of the results.

Overall both experimental techniques used in this study confirm that labyrinth metamater-

ials can be specially designed to control both transmission loss and dispersion characteristics across a broad frequency range, meaning this form of metamaterial possesses the ability to be used in a broad number of applications.

Numerical simulation of the experimentaly studied metamaterials is carried out using COMSOL software, in order to compare and validate both results and to improve our understanding of the acoustic behaviour of the various configurations tested here. The 3D model of the hybrid metamaterial was constrtucted and simulated on COMSOL in order to verify the absorption coefficient measured experimentally. The trend of the absorption coefficient showed a good agreement with the experiments in both 1 mm and 4 mm cases. The simulations also provided useful information about the nature of absorptivity indicating the areas of thermo-viscous losses that take place in the ducts of the absorber.

The numerical study of the labyrinth metamaterials reproduced both the extraordinary results of Xie et al. as well as our experimental. The transmission loss of different labyrinth unit designs was also tested and appeared to agree with the measurements for the original design but not so well for the rest. This suggests further experimental and numerical work needs to be carried out.

Numerical simulations provided an initial understanding of how one or more units of the same design affect the phase of the 1D wave, which lead to the reproduction of similar and even larger transmission angle with Xie et al. but with an array of units with completely different geometrical design (Redesign 2), which is also validated experimentally. It can therefore be assumed that similar negative refraction can be achieved with careful engineering of the row phase gradient.

Finally, an analytical model was developed in order to describe and approximate the space-coiling capabilities of single zig-zag metamaterial units. The the reflected wave amplitudes generally agreed with the numerical results for low frequencies up to 5 kHz. However, as frequency increases, the deviation between the results becomes greater, due to the increasing inefficiency of the computational mesh for accurate numerical simulation on the one hand, and to the lack of higher modal analysis of the present analytic model on the other. Therefore, the analytical model, being much faster than the numerical simulation, could be implemented for multi-parametric design optimisation of such units, but further numerical simulations are required to fully discover its capabilities. This could enable the engineering of more compact and efficient labyrinth structures, with less material and improved phase manipulation of a sound wave using zig-zag units.

While this study has made good progress in developing the understanding of acoustic metamaterials, the following points are recommended for further study.

For Heterogeneous Metamaterials:

- Investigate using different materials to construct resonators.
- Optimise multi-band HG metamaterials to improve broadband absorption.

For Hybrid Metamaterials:

- Use more advanced manufacturing methods to properly replicate Tang et al.'s design. Further improvements could then be suggested also based on the numerical results obtained by simulation software, using fine meshes and modelling all additional losses (thermal and viscous).

For Labyrinth Metamaterials:

- Test more unit cell designs in an impedance tube, accompanied by numerical methods. The aim of which is to develop a better understanding of the disagreements between experimental and numerical results as well as the physics behind what causes high transmission loss.
- Scale up unit cells to examine whether overall dimensions have an effect on location and magnitude of transmission loss peaks.
- Continue both unit cell and large scale structural changes on prisms at different frequencies to better understand negative refraction.
- Revise the explanation for the higher negative index of Improved design and generalise the phase gradient requirements for higher negativity of such array configurations.
- Extend the analytical model to describe open-end labyrinthine units and introduce modal analysis. Perform further parametric studies for the design optimization of such geometries, along with experimental and numerical validation.

Overall, this study has helped to develop the basic understanding of heterogeneous, hybrid and labyrinth metamaterials. The gained experience and the produced results can contribute to the development of the relatively new field of acoustics metamaterials, which will no doubt be the future of noise and vibration control.

8 References

[1] N. Kaina, F. Lemoult, M. Fink, and G. Lerosey. Negative refractive index and acoustic superlens from multiple scattering in single negative metamaterials. *Nature*, 525(7567): 77, 2015.

[2] B. Popa, L. Zigoneanu, and S. Cummer. Experimental acoustic ground cloak in air. *Physical review letters*, 106(25):253901, 2011.

[3] H. Ge, M. Yang, C. Ma, M. Lu, Y. Chen, and N. Fang. Breaking the barriers: Advances in acoustic functional materials. *National Science Review*, 5(2):159182, 2017.

[4] G. Ma and P. Sheng. Acoustic metamaterials: From local resonances to broad horizons. *Science advances*, 2(2):e1501595, 2016.

[5] Z. Liang and J. Li. Extreme acoustic metamaterial by coiling up space. *Physical review letters*, 108(11):114301, 2012.

[6] K. Idrisi. *Heterogeneous (HG) blankets for improved aircraft interior noise reduction*. PhD thesis, Virginia Tech, 2008.

[7] Y. Tang, S. Ren, H. Meng, F. Xin, L. Huang, T. Chen, C. Zhang, and T. Lu. Hybrid acoustic metamaterial as super absorber for broadband low-frequency sound. *Scientific Reports*, 7:43340, 2017.

[8] J. Groby, C. Lagarrigue, B. Brouard, O. Dazel, V. Tournat, and B. Nennig. Using simple shape three-dimensional rigid inclusions to enhance porous layer absorption. *The Journal of the Acoustical Society of America*, 136(3):1139–1148, 2014.

[9] A. Slagle and C. Fuller. *Low Frequency Noise Reduction Using Novel Poro-Elastic Acoustic Metamaterials*. PhD thesis, Virginia Tech, 2014.

[10] V. Jordan. The application of helmholtz resonators to sound-absorbing structures. *The Journal of the Acoustical Society of America*, 19(6):972–981, 1947.

[11] I. Romadhona and I. Yahya. On the use of coupled cavity helmholtz resonator inclusion for improving absorption performance of wooden sound diffuser element. *Procedia Engineering*, 170:458–462, 2017.

[12] D. Zhao and A. Morgans. Tuned passive control of combustion instabilities using multiple helmholtz resonators. *Journal of sound and vibration*, 320(4-5):744–757, 2009.

[13] A. Komkin, M. Mironov, and A. Bykov. Sound absorption by a helmholtz resonator. *Acoustical Physics*, 63(4):385–392, 2017.

[14] J. Groby, C. Lagarrigue, B. Brouard, O. Dazel, V. Tournat, and B. Nennig. Enhancing the absorption properties of acoustic porous plates by periodically embedding helmholtz resonators. *The Journal of the Acoustical Society of America*, 137(1):273–280, 2015.

[15] A. Nia and M. Sadeghi. The effects of foam filling on compressive response of hexagonal cell aluminum honeycombs under axial loading-experimental study. *Materials & Design*, 31(3):1216–1230, 2010.

[16] F. Côté, V. Deshpande, N. Fleck, and A. Evans. The compressive and shear responses of corrugated and diamond lattice materials. *International Journal of Solids and Structures*, 43(20):6220–6242, 2006.

[17] B. Han, W. Wang, Z. Zhang, Q. Zhang, F. Jin, and T. Lu. Performance enhancement of sandwich panels with honeycomb–corrugation hybrid core. *Theoretical and Applied Mechanics Letters*, 6(1):54–59, 2016.

[18] B. Han, K. Qin, B. Yu, B. Wang, Q. Zhang, and T. Lu. Honeycomb–corrugation hybrid as a novel sandwich core for significantly enhanced compressive performance. *Materials & Design*, 93:271–282, 2016.

[19] J. Arenas and M. Crocker. Recent trends in porous sound-absorbing materials. *Sound & vibration*, 44(7):12–18, 2010.

[20] A. Krushynska, F. Bosia, M. Miniaci, and N. Pugno. Spider web-structured labyrinthine acoustic metamaterials for low-frequency sound control. *New Journal of Physics*, 19(10): 105001, 2017.

[21] Y. Xie, B. Popa, L. Zigoneanu, and S. Cummer. Measurement of a broadband negative index with space-coiling acoustic metamaterials. *Physical review letters*, 110(17):175501, 2013.

[22] C. Liu, B. Xia, and D. Yu. The spiral-labyrinthine acoustic metamaterial by coiling up space. *Physics Letters A*, 381(36):3112–3118, 2017.

[23] T. Frenzel, J. David Brehm, T. Buckmann, R. Schittny, M. Kadic, and M. Wegener. Three-dimensional labyrinthine acoustic metamaterials. *Applied Physics Letters*, 103(6): 061907, 2013.

[24] Z. Liang, T. Feng, S. Lok, F. Liu, K. Ng, C. Chan, and et al. Space-coiling metamaterials with double negativity and conical dispersion. *Scientific reports*, 3:1614, 2013.

[25] D. Torrent and VM Garc. Quasi-two-dimensional acoustic metamaterials for sound control in ducts. 2013.

[26] T. Huang, C. Shen, and Y. Jing. Membrane-and plate-type acoustic metamaterials. *The Journal of the Acoustical Society of America*, 139(6):3240–3250, 2016.

[27] Y. Gu, Y. Cheng, J. Wang, and X. Liu. Controlling sound transmission with density-near-zero acoustic membrane network. *Journal of Applied Physics*, 118(2):024505, 2015.

[28] S. Maurya, A. Pandey, S. Shukla, and S. Saxena. Double negativity in 3d space coiling metamaterials. *Scientific reports*, 6:33683, 2016.

[29] A. Díaz-Rubio and S. Tretyakov. Acoustic metasurfaces for scattering-free anomalous reflection and refraction. *Physical Review B*, 96(12):125409, 2017.

[30] L. Wu, T. Chiang, C. Tsai, M. Wu, and L. Chen. Design of an acoustic bending waveguide with acoustic metamaterials via transformation acoustics. *Applied Physics A*, 109(3):523–533, 2012.

[31] Y. Li, X. Jiang, R. Li, B. Liang, X. Zou, and L. Yin. Experimental realization of full control of reflected waves with subwavelength acoustic metasurfaces. *Physical Review Applied*, 2(6):064002, 2014.

[32] Y. Xie, W. Wang, H. Chen, A. Konneker, B. Popa, and S. Cummer. Wavefront modulation and subwavelength diffractive acoustics with an acoustic metasurface. *Nature communications*, 5:5553, 2014.

[33] S. Lee, A. Shiouxios, and C. Chung. On the application of poroelastic metamaterials for noise reduction, 2017.

[34] ASTM Standard. Standard test method for impedance and absorption of acoustical materials using a tube, two microphones and a digital frequency analysis system. *ASTM Standard E*, 1990.

[35] ASTM Standard. Standard test method for normal incidence determination of porous material acoustical properties Based on the transfer matrix method. *ASTM Standard E*,

2017.

[36] L. Zigoneanu, B. Popa, and S. Cummer. Design and measurements of a broadband two-dimensional acoustic lens. *Physical Review B*, 84(2):024305, 2011.

[37] D. Bies, C. Hansen, and C. Howard. *Engineering noise control*. CRC press, 2017.

[38] COMSOL Multiphysics. Acoustic module–users guide, 2013.

[39] M. Han. *Sound reduction by a Helmholtz resonator*. PhD thesis, Lehigh University, 2008.

[40] E. Webster and C. Davies. The use of helmholtz resonance for measuring the volume of liquids and solids. *Sensors*, 10(12):10663–10672, 2010.

[41] P. Morse and K. Ingard. *Theoretical acoustics*. Princeton university press, 1968.

[42] Y. Li, B. Liang, Z. Gu, X. Zou, and J. Cheng. Reflected wavefront manipulation based on ultrathin planar acoustic metasurfaces. *Scientific reports*, 3:2546, 2013.